20
Modelling short fibre polymer reinforcements for composites

P. LAURE, Université de Nice-Sophia Antipolis, France and
L. SILVA and M. VINCENT, Mines-ParisTech, France

Abstract: The chapter is focused on fibre-reinforced thermoplastics. The fibre reinforcement improves their mechanical properties but the fibre orientation which results from the injection moulding process has a major influence. The chapter contains results of experimental observations of fibre length distribution, concentration and orientation for complex enough situations in order to describe problems encountered in real industrial processes. Then, the models which allow describing the evolution of fibre orientation in a flow motion are exposed. Finally, computations are made with an injection moulding simulation tool (Rem3D) in which these models are available. The comparison with experimental data concerning fibre orientation prediction gives information on the validity and the influence of various parameters associated with these models.

Key words: thermoplastic composite, reinforced polymers, fibre orientation, finite element computation.

20.1 Introduction

The chapter is focused on fibre-reinforced thermoplastics. There are two types of materials. Short fibre-reinforced pellets are obtained by mixing glass fibres and a thermoplastic matrix, polypropylene or polyamide for instance. The fibre content is usually between 30 and 50 wt%. The fibre length is distributed around a mean value of 500 μm. Long fibre-reinforced pellets are obtained by continuous impregnation of a fibre, by a pultrusion-like process. After solidification, the impregnated fibres are cut at a length around 10 mm. The fibre length is the same as the pellet length. Both materials are semi-product, adapted for fast production processes such as injection moulding or extrusion.

As with any composite, their properties are a function of the properties of the matrix, the fibres and the interface between matrix and fibres, but also of the fibre microstructure. This notion covers first the fibre orientation. Indeed, fibres get oriented by the flow, and their properties are anisotropic. It also covers the fibre length: it depends on the initial fibre length in the pellet, but also on the plasticising and injection steps of the process. Lastly, there is the fibre concentration, which is usually around 30–50 wt%, that is, about

half in volume for glass fibres, according to the glass and polymer densities. But the transport of the fibres by the polymer may be heterogeneous and fibre-rich or fibre-poor regions may be found.

The second section of this chapter reviews the experimental observations, and the variations of fibre length distribution, fibre concentration and orientation are discussed. The experimental procedures giving these data are also briefly described. The third section presents the models describing the evolution of fibre orientation in the flow motion. The most recent models which deal with concentrated suspensions are also discussed, as well as the coupling with the rheological behaviour. Finally, numerical computations are performed on three typical examples and the influence of various parameters encountered in the models is analysed. Then, the limitations of these models for real parts are discussed.

20.2 Observations

20.2.1 Fibre length distribution

As mentioned before, fibre length in the moulding depends on the initial fibre length in the pellet, and on the fibre degradation in the screw-barrel system of the plasticising unit and in the mould cavity.

Most methods for measuring fibre length are destructive (Kamal *et al.*, 1986; Chin *et al.*, 1988; Franzen *et al.*, 1989; Gupta *et al.*, 1989; Denault *et al.*, 1989; Akay *et al.*, 1995; Avérous *et al.*, 1997; Davidson and Clarke, 1999). The composite matrix is dissolved or burnt out. The fibre lengths are measured by image analysis of microscope pictures. The number of fibres is large (nearly 3000 per mm^3 for 30 wt% and fibres 300 μm long and 15 μm in diameter!) and a careful representative selection must be made. The image analysis technique must be able to take into account a large length distribution.

Glass fibre breakage is more important in the plasticising unit (Gupta *et al.*, 1989) than downstream in the runner and mould cavity. It is a function of fibre concentration (Denault *et al.*, 1989; Akay *et al.*, 1995; Tremblay *et al.*, 2000).

Vincent (2009) measured the fibre length distribution in a plaque mould for two reinforced polypropylenes, containing 30 wt% of short glass fibres and 30 wt% of long glass fibres (Fig. 20.1). The average length of the long fibres, initially 12 mm, reduces to 0.87 mm. The short fibre length, initially 0.56 mm, reduces to 0.41 mm. Fibre breakage for the long-fibre composite is important.

Figure 20.2 shows a plaque 150 × 150 × 3 mm, with seven ribs 25 mm apart from each other. The rib thicknesses from the entrance to the tip are 1, 3, 3, 2, 2, 3 and 3 mm. The rib heights are 9, 12, 9, 12, 9, 12 and 9 mm.

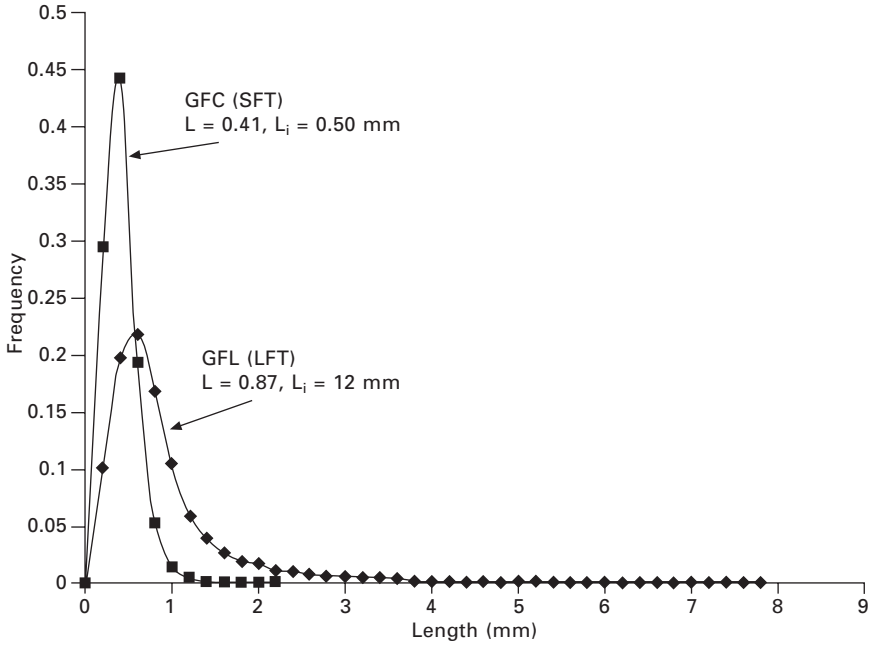

20.1 Fibre length repartition in a 30 wt% long and short glass fibre-reinforced polypropylene moulded plaque.

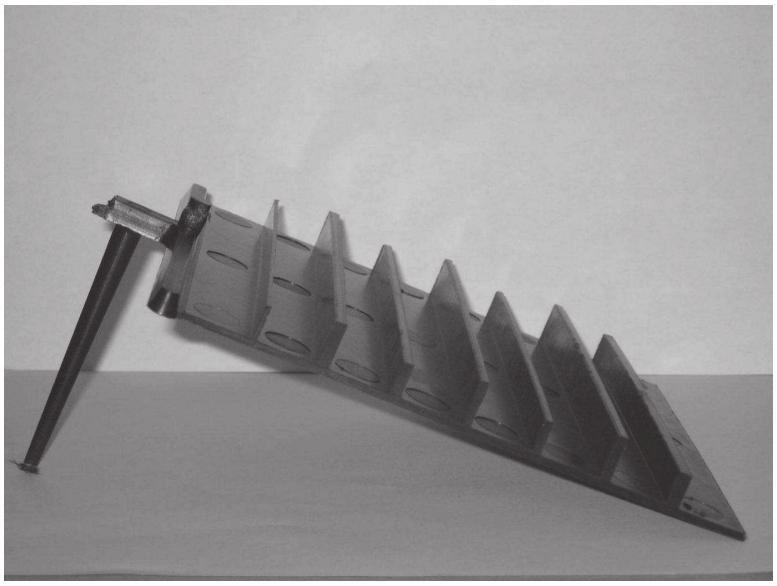

20.2 Geometry of the plaque with seven ribs: the size is 150 mm × 150 mm × 3 mm and the ribs are spaced at 25 mm.

The material is a 40 wt% long glass fibre reinforced polypropylene (pellet length 12 mm). Table 20.1 shows the average length at different positions for two mould filling flow rates. There is not a large difference between the rib and other regions in the part. The average length reduces by about 20% along the flow direction. The sensitivity to the flow rate is negligible.

20.2.2 Fibre concentration

Most authors have found small variations along the flow direction, around 1 to 2 wt% for a total amount of fibres of 30 wt% (Hegler and Menning, 1985; Kubat and Szalanczi, 1974). In the thickness directions, the fibre concentration is higher in the core than in the skin of the moulding, especially for a high fibre loading of 50 wt% (Kamal *et al.*, 1986; Akay and Barkley, 1991).

For the same part shown in Fig. 20.2, and with the same material, Fig. 20.3 shows the fibre concentration. The concentration is higher in the ribs, except in the first one, than in the plaque, but overall the deviation from the concentration of the semi-product, 40 wt%, is not very large.

20.2.3 Fibre orientation

Fibre orientation depends on the type of flow. In a shear flow, a single fibre rotates, but spends most of the time aligned with the flow direction. In a

Table 20.1 Average length in μm for different positions in the part shown in Fig. 20.2

Position	$Q = 9\ cm^3 \cdot s^{-1}$	$Q = 122\ cm^3 \cdot s^{-1}$
First rib	1200	1300
Plaque near first rib	1200	1300
Plaque between fourth and fifth ribs	1000	900
Plaque near fifth rib	900	1000
Fifth rib	1000	1000

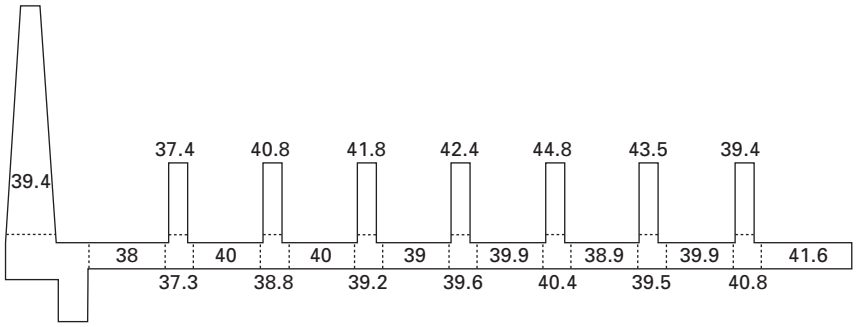

20.3 Fibre weight concentration (wt%) in the part shown in Fig. 20.2.

highly concentrated suspension, when fibres are interacting, fibres are mostly oriented in the flow direction. In an elongational flow, fibres get oriented in a stable position either parallel to the flow with a positive elongation rate, or perpendicular with a negative elongation rate. Interactions with neighbouring particles may disturb this orientation. In a real cavity filling situation, the flow is a complex combination of shear and elongation. Shear reaches a maximum in the skin, and elongation in the core. Elongation always occurs at the junction between the sprue or runners and the cavity itself, because the cross-section of the flow increases. This is why a skin–core structure is often observed in this region. Downstream, if the flow is shear dominated, fibres in the centre are reoriented in the flow direction, but the core region may appear again in case of increase of cross-section.

Figure 20.4 shows polished cross-sections of long glass fibre mouldings. In the surface, fibres appear mainly oriented in the flow direction, whereas in the centre, they are perpendicular to it. They are mostly parallel to the plan of the part. Short fibre composites show the same type of orientation. When the fibres are long enough, more than around 500 μm, they can be slightly curved. Otherwise, they appear as straight rods.

In order to be precise about the orientation, it is necessary to quantify it. The fibre orientation distribution function $\psi(\mathbf{p}, t)$ is defined by the probability $\psi(\mathbf{p}, t)\,\mathrm{d}\mathbf{p}$ of finding a fibre oriented between $\mathbf{p}$ and $\mathbf{p} + \mathrm{d}\mathbf{p}$, where $\mathbf{p}$ is a unit vector aligned with a fibre (Prager, 1957). The second-order orientation tensor $\boldsymbol{a}_2$ is easier to use in comparing two orientation patterns (Hand, 1961). It is defined as the spatial average of the double tensorial product of $\boldsymbol{p}$, and it is symmetrical and positive definite:

$$a_{ij} = \int_{\mathbf{p}} \psi(\mathbf{p}, t) p_i p_j \,\mathrm{d}\mathbf{p} \qquad 20.1$$

The trace of the tensor is equal to 1. For random orientation in space, the diagonal terms are equal to 1/3, and for random planar orientation, to 1/2. For perfect orientation in direction i, $a_{ii} = 1$, and the other diagonal values are zero. A diagonal tensor means that the reference frame axes are the principal axes of the tensor.

In order to obtain the orientation distribution function ψ or the second-order orientation tensor components, each fibre orientation in a given volume must be determined. Several techniques can be used (see, for instance, Clarke and Eberhardt, 2002 for a review), but the most widely used is to observe carefully polished cross-sections, such as those shown in Fig. 20.4. Cylindrical fibres making a certain angle with respect to the cutting plane appear as ellipses. The measurement of the orientation and length of the semi-axes of the ellipse leads to the vector $\mathbf{p}$ components in 3D. The image analysis technique must be accurate enough to separate touching fibres or to measure nearly circular fibre cross-sections, and corrections must be

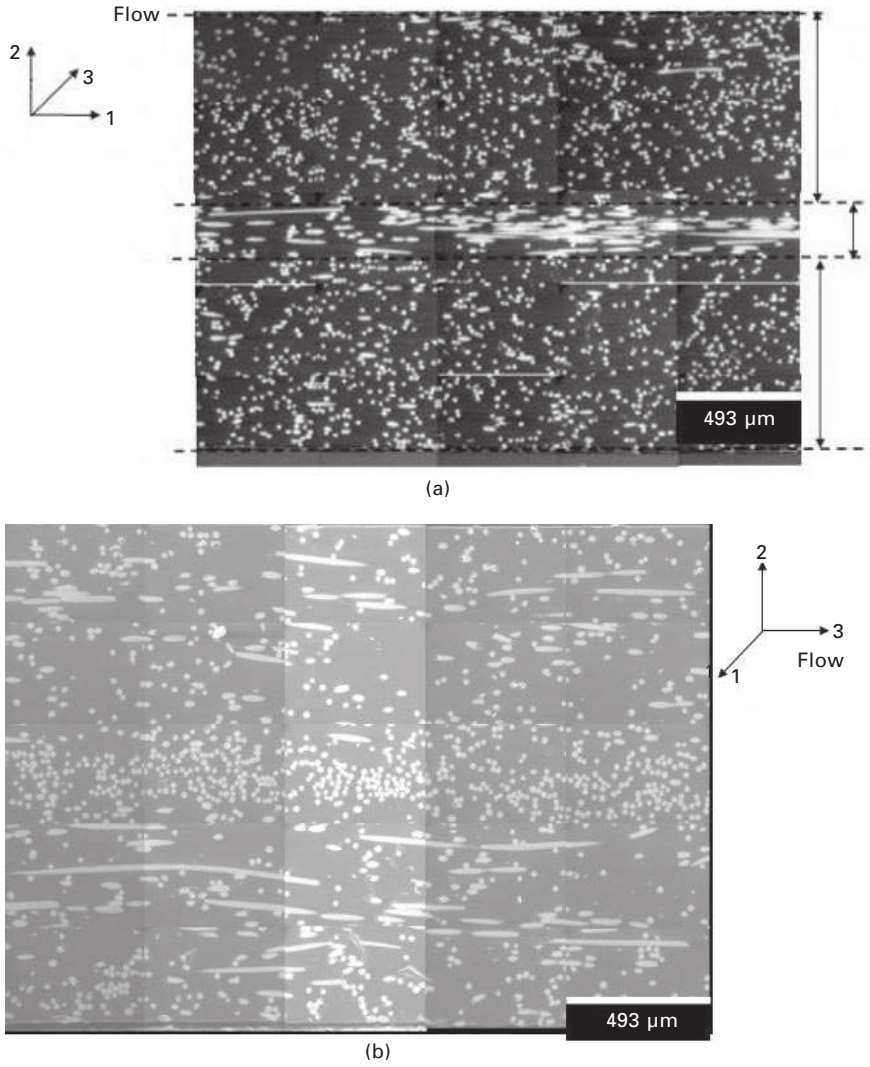

20.4 Pictures of a short fibre-reinforced polymer moulded plaque. The thickness is in the vertical direction: (a) flow direction perpendicular to observation plane; (b) flow direction parallel to large side of picture.

applied for long fibres for which the probability of intersecting the edge of the observed field is higher. Another important correction is necessary because the probability of observing fibres perpendicular to the observation plane is higher than when they are parallel to it (Bay and Tucker, 1992).

Other techniques can be used, such as confocal laser scanning microscopy (Eberhardt and Clarke, 2001) and X-ray microtomography (Shen *et al.*, 2004).

This last technique allows the 3D reconstruction of the fibres in a given volume. It is very powerful, as not only fibre orientation but also length, local concentration and eventually curvature can be evaluated.

20.2.4 Skin–core structure

A review of observations in various part geometries, such as plaque or centre gated discs, with different composites can be found in Papathanasiou (1997). The skin–core structure is often observed, the relative thickness of the skin and core layers depending on the processing conditions. At the flow front, fibres are mostly tangential to the front. This is why weld line regions exhibit weaker mechanical properties.

Figure 20.5 shows the gapwise evolution of the orientation tensor component in the flow direction, in a 50 wt% glass fibre reinforced polyarylamide plaque, for four cavity thicknesses (Vincent *et al.*, 2005; Vincent, 2009). The skin–core structure exists for the two largest thicknesses, but vanishes for the smallest ones. The shape of the plaque entrance, where the core is created, and the high shear rate generated by a small flow gap are responsible for this difference.

20.3 Models

20.3.1 Fibre orientation: Jeffery theory

Jeffery (1922) considered a single rigid ellipsoidal particle with very small dimensions. Thus, rate of deformation can be considered as homogeneous

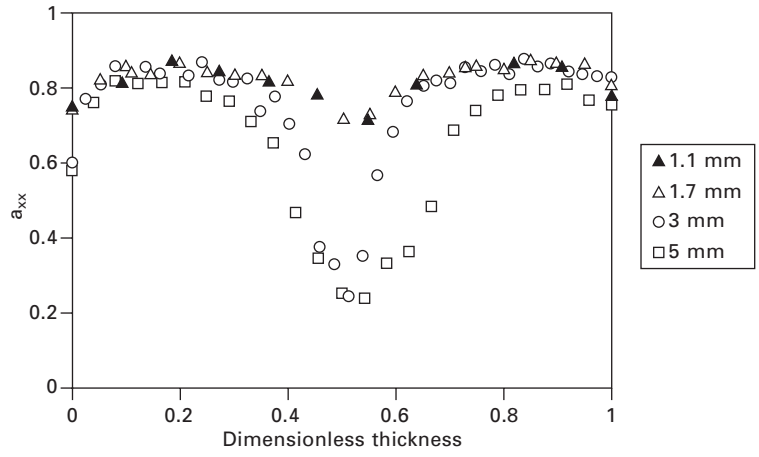

20.5 Orientation tensor component in the flow direction for four plaque thicknesses from 1.1 to 5 mm (after Vincent, 2009).

around the particle, and he supposed that this particle was immersed in a Newtonian fluid. The following time evolution equation of the unit vector $\boldsymbol{p}$ aligned with the particle axis was thus obtained:

$$\frac{\mathrm{d}p}{\mathrm{d}t} = \Omega\, p + \lambda[\dot{\varepsilon} p - (\dot{\varepsilon}\!:\! p \otimes p)\, p] \tag{20.2}$$

where $\dot{\varepsilon}$ is the rate of strain tensor and Ω is the vorticity tensor, both defined as functions of $\boldsymbol{v}$, the velocity field:

$$\dot{\varepsilon}(v) = \tfrac{1}{2}(\nabla v + \nabla v^t) \tag{20.3}$$

$$\Omega(v) = \tfrac{1}{2}(\nabla v - \nabla v^t) \tag{20.4}$$

λ is a function of the aspect ratio of the particle $\beta = L/D$, with L the length and D the diameter of the fibre:

$$\lambda = \frac{\beta^2 - 1}{\beta^2 + 1} \tag{20.5}$$

Typically, short fibres have a diameter between 10 and 20 μm, and a length between 100 and 500 μm, so that β is of the order 5 to 50, and λ is larger than 0.92.

In this theory, a particle rotates periodically in a simple shear flow, with a period of rotation of

$$T_{\mathrm{f}} = \frac{2\pi}{\dot{\bar{\varepsilon}}}\left(\beta + \frac{1}{\beta}\right) \tag{20.6}$$

where $\dot{\bar{\varepsilon}} = \sqrt{2\sum_{i,j} \dot{\varepsilon}_{ij}^2}$ is the is the magnitude of the strain rate tensor. This relation has been experimentally validated (Moses *et al.*, 2001). If the particle is infinitely long (slender body), the particle does not rotate any more but tends to orient in the flow direction. In elongation flows, equation 20.2 shows that a particle tends to a stable equilibrium position, parallel or perpendicular to the flow direction when the elongational rate is positive or negative, respectively. The kinetics of orientation are almost independent of the fibre aspect ratio when it is high. Later, Bretherton (1962) theoretically demonstrated that any rigid body of revolution has a motion in shear flow identical to an ellipsoid, meaning that the theory could be extended to fibre motion.

20.3.2 Fibre orientation: Folgar–Tucker model

Jeffery's equation is valid for dilute suspensions, when the fibre volume fraction $\phi \ll 1/\beta^2$. In the semi-concentrated regime, $1/\beta^2 \ll \phi \ll 1/\beta$,

hydrodynamic fibre interactions occur, whereas in the concentrated regime ($\phi \gg 1/\beta$), fibre–fibre contacts also appear. Fibre-reinforced thermoplastics are often in this latest regime.

Since in the concentrated regime one cannot follow each fibre, the orientation distribution function, $\psi(\mathbf{p}, t)$, defined in the previous section, is used. The equation of conservation of ψ is of the Fokker–Planck type and is written (by neglecting fibre Brownian motion, in the dilute case)

$$\frac{\partial \psi}{\partial t} + \frac{\partial}{\partial p}\left(\psi \frac{\mathrm{d}p}{\mathrm{d}t}\right) = 0 \qquad 20.7$$

For concentrated regimes, one introduces a pseudo-Brownian diffusion, giving

$$\frac{\partial \psi}{\partial t} + \frac{\partial}{\partial p}\left(\psi \frac{\mathrm{d}p}{\mathrm{d}t}\right) = D_\mathrm{r} \frac{\partial^2 \psi}{\partial p^2} = 0 \qquad 20.8$$

The distribution function is a complete and accurate representation of the orientation state. However, solving this equation requires significant computational resources, and for industrial applications, it is better and easier to use the second-order orientation tensor, $\boldsymbol{a}_2$, defined in equation 20.1. Passing from an orientation distribution function $\psi(\mathbf{p}, t)$ to $\boldsymbol{a}_2$ implies a loss of information. Thus, one may use higher-order tensors, such as $\boldsymbol{a}_4$, the fourth-order orientation tensor:

$$\boldsymbol{a}_4 = \int_p p \otimes p \otimes p \otimes p \, \psi(p) \mathrm{d}p \qquad 20.9$$

and may reconstruct $\psi(p, t)$, as suggested by Advani and Tucker (1987), from both tensors.

To directly solve orientation motion based on the second-order orientation tensor, Lipscomb *et al*. (1984) provided the following equation, after volume averaging:

$$\frac{\mathrm{d}a_2}{\mathrm{d}t} = \Omega a_2 - a_2 \Omega + \lambda(\dot{\varepsilon} a_2 + a_2 \dot{\varepsilon} - 2\dot{\varepsilon}{:}a_4) \qquad 20.10$$

For concentrated solutions, Folgar and Tucker (1984) chose a phenomenological approach. They added a term to Jeffery's equation using an analogy with rotary Brownian diffusion to account globally for these complex interactions. They obtained:

$$\frac{\mathrm{d}a_2}{\mathrm{d}t} = \Omega a_2 - a_2 \Omega + \lambda(\dot{\varepsilon} a_2 + a_2 \dot{\varepsilon} - 2\dot{\varepsilon}{:}a_4) + 2C_\mathrm{I}\dot{\bar{\varepsilon}}(I - 3a_2) \qquad 20.11$$

where C_I is an empirical constant called the interaction coefficient.

This model has been extensively used, and is the standard model. Two

questions arise when treating this equation: how to compute $\boldsymbol{a}_4$ from $\boldsymbol{a}_2$? And what are the admissible values for C_I?

Closure approximations

The fourth-order tensor $\boldsymbol{a}_4$ appears in the time evolution equation for $\boldsymbol{a}_2$, thus a closure approximation is needed to approximate $\boldsymbol{a}_4$ as a function of $\boldsymbol{a}_2$ (since to compute $\boldsymbol{a}_4$, one needs also $\boldsymbol{a}_6$). Tests carried out in simple flows (shear, elongation, or a simple combination of both) showed that the closure approximation has a large influence on the quality of the result. The simplest approximations are the quadratic closure (which gives exact results when fibres are perfectly aligned) and the linear closure (exact for random orientation). The hybrid approximation is a linear combination, depending on the orientation, of the two previous ones (Advani and Tucker, 1987).

One other class of closure approximations includes fitted parameters in simple flows, like the orthotropic (Cintra and Tucker, 1995; Wetzel and Tucker, 1999) or the natural closures (Dupret and Verleye, 1998). In these approaches, the fourth-order tensor is written as a linear function of the invariants of the second-order orientation tensor. Coefficients of the different functions corresponding to each approximation are obtained by fitting to the analytical solution of the steady-state orientation distribution function for several flow situations: shear, elongation and combinations of both. Performance studies of closure approximations in shear flows show that linear closures may provide non-physical oscillations, which does not happen with quadratic or hybrid closures. The transient state is generally overestimated (with longer times), whereas the stationary one is underestimated (with shorter times); fibre alignment prediction is very unidirectional. In elongation flows, linear closure may also give unrealistic values, whereas quadratic or hybrid approximations provide better results, even if they overestimate the transient region. Orthotropic closures always provide the best results and are the most commonly used.

Interaction coefficient: theoretical, numerical and experimental determination

For shear flows, the interaction coefficient value is very important in making good predictions of the steady-state solution of the orientation tensor: if C_I is high, the orientation becomes isotropic, whereas for a weak C_I, fibres tend to align in the flow direction. On the other hand, in elongation flows, C_I influences the orientation transient solution: if C_I is high, fibre orientation attains the steady state more rapidly than for lower values.

In a shear flow, when C_I is around 10^{-4}, a_{11} is close to 1, meaning that fibres are very well oriented in the flow direction. When C_I increases, a_{11}

decreases, and for $C_I = 1$ the orientation becomes nearly isotropic ($a_{11} = 1/3$). The fibre aspect ratio β has a negligible influence on the steady-state attained value, even though Hinch and Leal (1973) showed that for very weak diffusion (a very small interaction coefficient) it may become important.

The value of C_I can be determined through theoretical, numerical or experimental fitting. In this last case, it can be difficult to find only one C_I that fits in the whole flow range. Bay and Tucker (1992) used an empirical approach, based on experimental values for injected discs and plaques for different polymers and concentrations, to propose:

$$C_I = 0.0814e^{-0.7148\phi\beta} \qquad 20.12$$

On the theoretical side, Ranganathan and Advani (1991) proposed a relationship between the interaction coefficient and the distance between fibres, h:

$$C_I = K\frac{L}{h} \qquad 20.13$$

where K is a constant determined experimentally and L is the fibre length.

Direct numerical simulation has also been used to estimate C_I values. Yamane *et al.* (1994) modelled fibre–fibre interaction for a Newtonian fluid in shear flow using lubrication forces. The authors obtained very low interaction coefficients ($10^{-7} < C_I < 10^{-4}$). Fan *et al.* (1998) developed a numerical approach to take into account fibre–fibre interactions, leading to an interaction coefficient that has a tensorial form, which will be discussed in the next section. Phan-Thien *et al.* (2002) extended the previous approach by using the trace of the interaction coefficient tensor, and they proposed the following form for C_I:

$$C_I = 0.03(1 - e^{-0.224\phi\beta}) \qquad 20.14$$

The values obtained seem of a good order of magnitude ($10^{-3} < C_I < 10^{-2}$). Furthermore, one obtains the interesting result that the interaction coefficient increases with the fibre volume fraction and the fibre aspect ratio. This is a point of discussion, since high volume fractions do not often lead to isotropic orientations, which are the result of Folgar and Tucker's model when one considers a high C_I. The models discussed in the next section will enlighten this fact.

20.3.3 Fibre orientation: recent models with anisotropic fibre interaction

In the previous standard model, an isotropic rotary diffusion term was added by Folgar and Tucker. The diffusivity is proportional to the magnitude of the rate of deformation (scalar), through the constant C_I. Experimental data has shown that, for concentrated suspensions, the kinetics of orientation are

much slower than are predicted by Folgar and Tucker's standard model. To avoid this effect, Wang *et al*. (2008) introduced the reduced strain closure (RSC) model. The authors write $\boldsymbol{a}_2$ as a function of its eigenvalues Λ_i and eigenvectors $\boldsymbol{e}_i$, and suppose that the eigenvalue kinetics are slowed by a factor of κ and that the eigenvector kinetics are unchanged. The tensorial material derivative of $\boldsymbol{a}_2$ is then recalculated, resulting in the following variation of the Folgar and Tucker model:

$$\frac{\mathrm{d}a_2}{\mathrm{d}t} = \Omega a_2 - a_2\Omega + \lambda(\dot{\varepsilon}a_2 + a_2\dot{\varepsilon} - 2\dot{\varepsilon}{:}[a_4 + (1+\kappa)(l_4 - m_4 a_4)]) + 2\kappa C_I\dot{\bar{\varepsilon}}(I - 3a_2) \quad 20.15$$

The fourth order tensors $\boldsymbol{l}_4$ and $\boldsymbol{m}_4$ are functions of the eigenvalues and eigenvectors of $\boldsymbol{a}_2$:

$$l_4 = \sum_{i=1}^{3} \Lambda_i(\mathrm{e_i e_i e_i e_i}) \quad 20.16$$

$$m_4 = \sum_{i=1}^{3} (\mathrm{e_i e_i e_i e_i}) \quad 20.17$$

Parameter κ is determined by fitting experimental data. For short fibre reinforced thermoplastics, it ranges from 0.05 to 0.2 (Wang *et al*., 2008). To avoid the use of closure approximations, Wang *et al*. (2008) have also derived a Fokker–Planck equation including this slow kinetics phenomenon. Nevertheless, it remains computationally expensive when compared with the tensorial form.

Using a different approach, Férec *et al*. (2009) obtained a similar model. The authors have considered that orientation kinetics become slower with semi-concentrated suspensions because of hydrodynamic and fibre–fibre interactions. The force generated by fibre interactions was modelled using a linear hydrodynamic friction coefficient proportional to the relative velocity at the contact point and weighted by the probability for contacts to occur. Starting from this point, the authors obtained the following orientation evolution equation:

$$\frac{\mathrm{d}a_2}{\mathrm{d}t} = \Omega a_2 - a_2\Omega + \lambda(\dot{\varepsilon}a_2 + a_2\dot{\varepsilon} - 2\dot{\varepsilon}{:}a_4) + \phi\widetilde{M}(\dot{\varepsilon}b_2 + b_2\dot{\varepsilon} - 2\dot{\varepsilon}{:}b_4) + 2f\phi\widetilde{M}q\dot{\bar{\varepsilon}}(I - 3a_2) \quad 20.18$$

where f is the average number of contacts per fibre, $\widetilde{M}$ is a parameter related to drag, and q is a dimensionless interaction coefficient. $\boldsymbol{b}_2$ and b_4 are the second-and fourth-order interaction tensors. $\boldsymbol{b}_2$ is given by

$$b_2 = \frac{3\pi}{8}(a_2 - a_4 : a_2) \tag{20.19}$$

and the fourth-order interaction tensor, $\boldsymbol{b}_4$, is computed from the second-order one through a quadratic closure approximation. Férec *et al*. (2009) have demonstrated that their model can be rewritten as a RSC model type.

Globally, the RSC model behaves well for short fibre reinforced materials. For long fibre thermoplastics, it quantitatively generates higher flow aligned fibres which do not agree with the experimental values. Thus, rotary diffusion models have been lately developed (Ranganathan and Advani, 1991; Fan *et al*., 1998; Phan-Thien *et al*., 2002; Koch, 1995; Phelps and Tucker, 2009). Ranganathan and Advani (1991) proposed a model in which the interaction coefficient is inversely proportional to the average interfibre spacing. Diffusion is isotropic and not really applicable to long fibre reinforced materials. Fan *et al*. (1998) and Phan-Thien *et al*. (2002) developed a rotary diffusion anisotropic model by replacing the interaction coefficient C_I by a second-order tensor C, computed by performing direct numerical simulations of a REV of a concentrated suspension undergoing a simple shear flow (Beaume, 2009). C was then determined using the steady-state solution, not exploiting dynamic behaviour. Koch (1995) obtained also an expression for the tensor C using a mechanistic approach, by considering the influence of hydrodynamic fibre–fibre interactions on the orientation development in the semi-dilute regime. This tensor is of the form

$$C = \frac{nL^3}{\dot{\bar{\varepsilon}}^2 \ln^2 \beta}[b_1(\dot{\varepsilon} : a_6 : \dot{\varepsilon})I + b_2(\dot{\varepsilon} : a_6 : \dot{\varepsilon})] \tag{20.20}$$

where n is the number of fibres per unit volume, b_1 and b_2 are parameters computed by fitting with analytical orientation values in elongation flows, and $\boldsymbol{a}_6$ is the sixth-order orientation tensor. The author was then led to the following orientation equation:

$$\frac{\mathrm{d}a_2}{\mathrm{d}t} = \Omega a_2 - a_2\Omega + \lambda(\dot{\varepsilon}a_2 + a_2\dot{\varepsilon} - 2\dot{\varepsilon} : a_4)$$

$$+ \dot{\bar{\varepsilon}}[2C - 2(\mathrm{tr}\, C)a_2 - 5(Ca_2 + a_2 C) + 10a_4 : C] \tag{20.21}$$

Since the sixth-order tensor needs to be computed, the Koch model is more computationally costly. It does not provide better results than Folgar and Tucker's model for long fibre reinforced thermoplastics, and the quality of results is also dependent on the ratio between b_1 and b_2 (if b_1 is much larger than b_2, diffusion becomes mostly isotropic and the model close to Folgar and Tucker's one).

Recently, Phelps and Tucker (2009) developed a phenomenological anisotropic rotary diffusion model, using also a second-order tensor to describe

interaction, by allowing the diffusion term to depend on the orientation state and on the rate of deformation tensor, using the final expression

$$C = b_1 I + b_2 a_2 + b_3 a_2^2 + \frac{b_4}{\dot{\bar{\varepsilon}}}\dot{\varepsilon} + \frac{b_5}{\dot{\bar{\varepsilon}}^2}\dot{\varepsilon}^2 \qquad 20.22$$

The five scalar parameters b_1, …, b_5 are fitted in order to get steady-state orientation solutions in simple shear flow and various elongation flows, ensuring stable-steady state positive eigenvalues, as well as physical solutions. The so-called ARD-RSC (anisotropic rotary diffusion – reduced strain closure) model is thus written:

$$\frac{\mathrm{d}a_2}{\mathrm{d}t} = \Omega a_2 - a_2\Omega + \lambda(\dot{\varepsilon}a_2 + a_2\dot{\varepsilon} - 2\dot{\varepsilon}:[a_4 + (1-\kappa)(l_4 - m_4 a_4)])$$

$$+\dot{\bar{\varepsilon}}(2[C-(1-\kappa)m_4:C]-2\kappa(\mathrm{tr}\,C)a_2 - 5(Ca_2 + a_2 C)$$

$$+10[a_4 + (1-\kappa)(l_4 - m_4 a_4)]:C\} \qquad 20.23$$

This latest model has been shown to be predictive for long fibre thermoplastic composites, even though there are a large number of parameters to fit.

20.3.4 Rheological models

Generic form with rheological coefficients N_p and N_s

In the most general case, we consider that the extra stress tensor is the sum of the contribution of the fluid and of the particles (Batchelor, 1971), and that a reinforced polymer is a suspension of rigid particles in a Newtonian fluid. In this case, most theories have derived the following expression for the stress tensor (Tucker, 1991):

$$\sigma = -pI + 2\eta_I[\dot{\varepsilon} + N_p\dot{\varepsilon}:a_4 + N_s(\dot{\varepsilon}a_2 + a_2\dot{\varepsilon})] \qquad 20.24$$

where η_I, N_p and N_s are parameters depending on the fluid viscosity, fibre aspect ratio, fibre orientation and fibre concentration. They can be obtained from rheological experiments that are difficult to perform in the concentrated case. On the other hand, theoretical expressions obtained for each of these parameters depend on the concentration domain. It is most often the dilute and semi-concentrated regime which limits greatly their wide application. Three type of approaches are used in the literature to obtain N_p and N_s: the slender body theory, where a particle is considered as an infinitely thin fibre (of negligible thickness) (Batchelor, 1971; Dinh and Armstrong, 1984; Shaqfeh and Fredrickson, 1990); the derivation of known results for suspensions of ellipsoidal particles, valid for finite fibre aspect ratios (Hinch and Leal, 1973; Lipscomb *et al.*, 1988; Hand, 1961); and the approximation based on the theory of Doi and Edwards for concentrated suspensions, where the Brownian

motion of the suspension is not neglected and a diffusion coefficient appears in the stress tensor expression. In all the above theories, N_p is larger than N_s for high aspect ratios.

Slender body approximation and ellipsoidal particle theories

In the approximations based on the slender body theory, η_I is equal to the fluid viscosity and $N_s = 0$. They are valid for dilute (for $\phi \ll 1/\beta^2$) (Batchelor, 1970) or for semi-concentrated suspensions (Batchelor, 1971; Dinh and Armstrong, 1984; Shaqfeh and Fredrickson, 1990). For dilute suspensions, Batchelor (1970) proposed the following expression:

$$N_p = \frac{\beta^2 \phi}{3 \ln(\beta)} \tag{20.25}$$

To extend the approach to the semi-concentrated regime, authors have considered hydrodynamic and fibre–fibre interactions, as well as lubrication forces. Hence, Batchelor (1971) gave

$$N_p = \frac{\beta^2 \phi}{9\left[\ln(2\beta) - \ln\left(1 + 2\beta\sqrt{\frac{\phi}{\pi}}\right) - 1.5\right]} \tag{20.26}$$

whereas Dinh and Armstrong (1984) considered the influence of orientation by providing N_p as

$$N_p = \frac{\beta^2 \phi}{3 \ln\left(\frac{2h}{D}\right)} \tag{20.27}$$

where h represents the characteristic distance between two neighbouring fibres, a distance that depends on the particles' orientation. A similar expression has been obtained by Shaqfeh and Fredrickson (1990). Ranganathan and Advani (1991) proposed a modification to the Batchelor (1970) model using a corrective factor function of the fibre aspect ratio, providing better results but very sensitive to this correction. Other expressions are based on ellipsoidal particle theories (Lipscomb *et al.*, 1988; Hinch and Leal, 1973) where N_s is different from zero but much smaller than N_p, and η_I is different from the fluid viscosity. For dilute suspensions, they take the form:

$$N_p = \frac{\phi}{1 + 2\phi} \frac{\beta^2}{2[\ln(2\beta) - 1.5]}$$

$$N_s = \frac{\phi}{1 + 2\phi} \frac{6\ln(2\beta) - 11}{\beta^2} \tag{20.28}$$

$$\eta_I = \eta(1 + 2\phi)$$

Extensions of this model have also been proposed, to improve the results when going towards the semi-concentrated regime.

Model with interaction tensor for concentrated suspension

Based on the work of Dinh and Armstrong (1984) for slender fibre suspensions, Férec *et al*. (2009) have derived the following expression for the total stress tensor, including a term that is a function of the interaction tensor:

$$\sigma = -pI + 2\eta_I[\dot{\varepsilon} + N_p\dot{\varepsilon}{:}a_4 + N_b\dot{\varepsilon}{:}b_4] \qquad 20.29$$

with

$$N_p = \frac{\phi D^2 X_A}{12\pi} \qquad 20.30$$

$$N_b = \frac{2\phi^2 D^2 K}{3\pi}$$

where X_A is the parallel drag coefficient to the fibres, dependent on the nature of the fibre–matrix contact, and k is a dimensionless geometric factor. For very low fibre volume fractions, N_b becomes insignificant and the total stress reduces to the Dinh and Armstrong (1984) model.

20.4 Computation of fibre orientation in injection moulding

We present computational examples of fibre orientation in injection moulding for which experimental data exist. The various moulds are geometrically complex enough to describe problems encountered in real industrial processes. In the first example, we check whether the skin–core effect is accurately computed in a rectangular plaque. Moreover, the influence of the orientation–rheology coupling and of the interaction coefficient C_I is analysed by computing the orientation near the inlet gate. The second example is a U-shape with thin walls and ribs, which is used in the automotive industry. It shows the ability to compute the appearance and location of weld lines. The third example is the plaque with seven different ribs (see Fig. 20.2) which gives information on the orientation state in small parts.

First of all, the numerical methods are briefly described. The methodology is that used in Rem3D software and is based on an Eulerian approach (the whole injection cavity is meshed) and a stabilised Galerkin method, using a continuous approximation of the orientation tensor coupled to flow (generalised Stokes behaviour), the thermal equation, the flow front evolution (using a level set method) and fibre orientation equations.

20.4.1 Numerical methods

A weakly coupled approach is used, meaning that the problem is solved in two steps. The first step involves the solution of the mechanical problem, assuming that the polymer is incompressible and neglecting gravity and inertia:

$$\nabla \cdot \sigma = 0, \quad \nabla \cdot v = 0 \tag{20.31}$$

with an isotropic orientation at the first step or an orientation tensor determined at the previous time step for the other instants. The orientation is taken into account through expression 20.24 or 20.29. A classical mixed finite element method (Pichelin and Coupez, 1998) is used, in which the orientation tensor is implicitly considered.

The fluid is assumed to follow an incompressible shear-thinning behaviour, represented by Carreau–Yasuda and Arrhenius laws for the viscosity η:

$$\eta = \eta_0(T)\left[1 + \left(\eta_0 \frac{\dot{\bar{\varepsilon}}}{\tau_c}\right)^{\alpha}\right]^{\frac{m-1}{\alpha}}, \ \eta_0(T) = \eta_0(T_{\text{ref}}) \exp\left[\beta_T\left(\frac{1}{T} - \frac{1}{T_{\text{ref}}}\right)\right] \tag{20.32}$$

The parameters occurring in these laws are given in Table 20.2 for the fluid studied.

As viscosity depends on temperature, the energy equation resolution is coupled and solved:

$$\rho C_p\left(\frac{\partial T}{\partial t} + u \cdot \nabla T\right) = \nabla \cdot (k_{\text{T}} \nabla T) + \eta \dot{\bar{\varepsilon}}^2 \tag{20.33}$$

where ρ is the volume density, C_p the specific heat, k_{T} the thermal conductivity, and the last term represents the viscous dissipation. These parameters are

Table 20.2 Parameters used in equations 20.32 and 20.33 for PAA50, Stamax P30YM240 and P40YM243: C_p is the specific heat, k is the thermal conductivity

	PAA50	P30YM240	P40YM243
τ_c	0.154 MPa	0.0411 MPa	0.02626 MPa
$\eta_0(T_{\text{ref}})$	570 Pa.s	252 Pa.s	636.6 Pa.s
α	0.55	1	1
m	0.3	0.22	0.271
T_{ref}	549 K	523 K	493 K
β_T	7764 mole.K	4450 mole.K	4450 mole.K
k_T	0.3 W/m.K	0.25 W/m.K	0.15 W/m.K
C_p	1766 J/kg.K	2180 J/kg.K	3100 J/kg.K
ρ	1522 kg/m^3	1000 kg/m^3	1000 kg/m^3

considered to be constant. Finally, heat conduction towards the mould walls and viscous heating are also taken into account.

The second step involves the computation of fibre orientation with velocity field obtained in the previous step, through the resolution of the evolution equation 20.11. Numerical resolution of Folgar and Tucker's equation has been performed by Kabanémi and Hétu (1999) using the fourth-order Runge–Kutta method, by Martinéz *et al*. (2003) with the method of characteristics, and by Pichelin and Coupez (1999) and Redjeb *et al*. (2005) with a space–time discontinuous Galerkin scheme. Miled *et al*. (2008) have proposed a standard Galerkin method associated with a RFB or SUPG stabilisation, which prevents inaccurate oscillations due to the hyperbolic character of this equation. A moving interface (such as fluid/air) is also calculated at each time step by solving a convection equation (Ville *et al*., 2010) associated with a signed distance function which defines the fluid domain (its value is positive in the fluid and negative in the empty region):

$$\frac{\partial \alpha}{\partial t} + v \cdot \nabla \alpha = 0 \qquad 20.34$$

Finally, all parameters and equations are extended to the whole computational domain, as the weak formulation of the finite element method ensures the continuity of stress, velocity, orientation tensor and temperature (Batkam *et al*., 2004).

20.4.2 Representation of orientation

The problem is now to get practical information from the computed orientation tensor. In an orthonormal Cartesian basis, the diagonal term a_{ii} of the orientation tensor quantifies the fibre alignment along the main axis. As already mentioned in the first section, $a_{11} = 1$ means that all the fibres are oriented along the direction $\boldsymbol{i}_1$. Moreover, $a_{11} = 0$ indicates that all the fibres are perpendicular to the axis $\boldsymbol{i}_1$, that is, they belong to the plane. ($\boldsymbol{i}_2$, $\boldsymbol{i}_3$). The components a_{ij} with $i \neq j$ quantify the asymmetry of the distribution of orientation relative to the direction i_i or i_j. For isotropic orientation in 3D, the components are $a_{ii} = \frac{1}{3}$ while $a_{ij} = 0$ for $i \neq j$.

Another way to describe the computed orientation is to plot the ellipsoid associated with the eigenvalues, $\boldsymbol{\Lambda}_i$, and eigenvectors, $\boldsymbol{e}_i$, of the orientation tensor $\boldsymbol{a}_2$ (Advani and Tucker, 1987; Altan *et al*., 1990). The eigenvectors and eigenvalues of the orientation tensor give, respectively, the direction and length axes of the ellipsoid as shown in Fig. 20.6.

In order to determine the degree of anisotropy, a von Mises effective orientation, a_v, can also be computed:

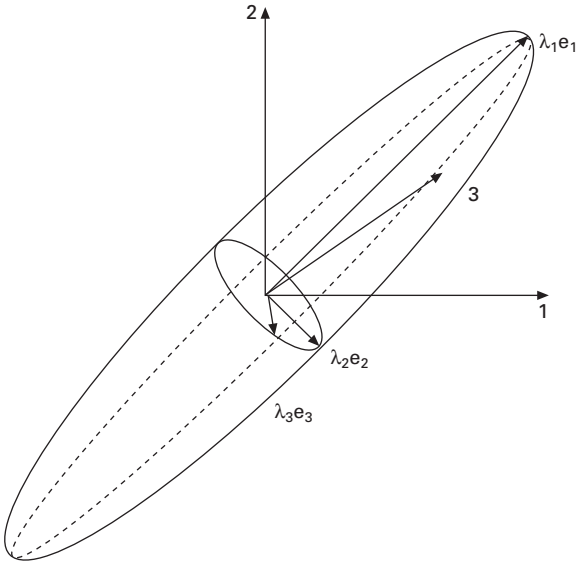

20.6 Ellipsoid representation of orientation tensor a_2.

$$a_v = \sqrt{\frac{(a_{11} - a_{22})^2 + (a_{22} - a_{33})^2 + (a_{11} - a_{33})^2 + 6(a_{12}^2 + a_{13}^2 + a_{23}^2)}{2}} \qquad 20.35$$

It is null for an isotropic orientation and 1 if all fibres are oriented along a principal direction.

20.4.3 Rectangular plaque with inlet gate

We consider the injection moulding of a three-dimensional plaque (Fig. 20.7(b)), and in particular we study the orientation development near the injection gate. Dimensions of the plaque are given in Fig. 20.7(a). Only half of the plaque will be considered in the simulation, since the geometry presents a symmetry plane.

The polymer is a polyarylamide (Solvay Ixef 1022) reinforced with 50% weight (31.6% volume) glass fibres. The fibre aspect ratio is considered constant and equal to 10. The injection is done at a flow rate of 20 cm^3/s and the initial polymer temperature is 270°C. The mould temperature is kept constant at 130°C, and the mould is filled in 2.70 s. The computational time step is 0.002 s. The orientation distribution is analysed after 1300 time iterations, almost at the end of cavity filling.

In order to reduce the computational time, the long circular channel has not been taken into account. The inlet of the cavity is just after the last curve

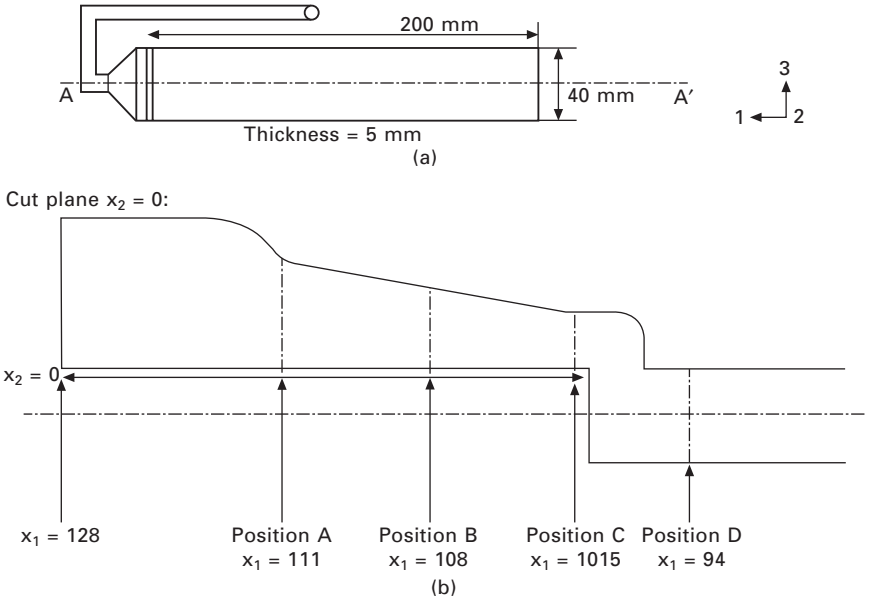

20.7 (a) Mould schematic view and (b) zoom on the inlet with positions of sensors.

of the feeding channel. The computations are made on a half-mould with symmetric boundary conditions on the plane ($\boldsymbol{i}_1$, $\boldsymbol{i}_2$). The problem is now to impose an initial orientation at the cavity inlet as we do not take into account the cylindrical channel. Usually one considers an isotropic initial orientation. But the flow in the channel is dominated by shear deformations, which are known to orient fibres mainly in the flow direction (namely the $\boldsymbol{i}_1$ axis) at the entrance of the triangular gate. Nevertheless, the two curves in the cylindrical channel can disturb this orientation. So, computations are made for two different initial conditions (isotropic case, $a_{ii} = \frac{1}{3}$; unidirectional case, $a_{11} = 1$) and a hybrid closure approximation. Moreover, two values of the interaction coefficient ($C_\mathrm{I} = 0.001$ and 0.04) and two values of the rheological coupling coefficients ($N_p = 0$, 100 and $N_s = 0$) will be tested.

Figure 20.8 shows cross-sections in the ($\boldsymbol{i}_1$, $\boldsymbol{i}_2$) plane at the end of filling and the distribution of the diagonal orientation tensor components. We notice that the tensor is almost diagonal, so the ($\boldsymbol{i}_1$, $\boldsymbol{i}_2$, $\boldsymbol{i}_3$) axes are the principal axes of the orientation tensor. Also, the skin–core effect initiated at the end of the gate is preserved until the end of the plaque. Computed values of a_{22} are very small, except at the junction between the divergent region and the plaque. This means that fibres are parallel to the ($\boldsymbol{i}_1$, $\boldsymbol{i}_3$) plane in the areas where experimental observations are made. This is in agreement with the observations, and we will focus on the a_{11} component which quantifies the

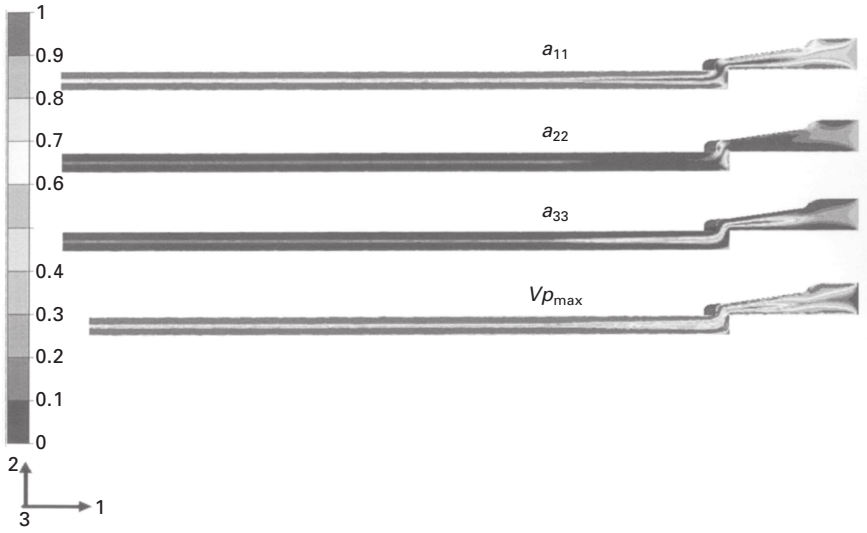

20.8 Isovalues of a_{11} at the end of filling in a cross-section (i_1, i_2, i_3 = 0) for the PAA50 with isotropic initial orientation, N_p = 0 and C_I = 0.001.

degree of alignment with the flow direction. The triangular gate region is divergent in the plane ($\boldsymbol{i}_1$, $\boldsymbol{i}_3$) and convergent in the plane ($\boldsymbol{i}_1$, $\boldsymbol{i}_2$) (see Fig. 20.7). The negative elongation rate along the $\boldsymbol{i}_3$ axis dominates over the positive one along the $\boldsymbol{i}_1$ axis and an orientation perpendicular to the $\boldsymbol{i}_1$ direction develops in the core. This orientation is transported at the junction between the gate and the plaque so that at the entrance of the plaque, we obtain a skin/core orientation, with a skin oriented in the flow direction, and a core perpendicular to it. These calculations show how a gate can lead to a skin/core structure in moulded parts. The computations are qualitatively in agreement with the observations.

In Fig. 20.9, the evolution of a_{11} with x_2, the plaque thickness, is shown at the four positions A, B, C and D where the experimental measurements were made (see Fig. 20.7(b)). Computations were performed with an isotropic initial orientation, showing the following:

1. A skin/core structure is rapidly formed in zone A, and it remains even in D after the junction gate-plaque. As shown in the experiments, the skin/core structure is less significant for position C than for position D.
2. For a partially coupled calculation (N_p = 0), when the interaction coefficient C_I increases, near the surface fibres are less oriented in the flow direction. For example, in the first position A for the lower wall (x_2 = 2.5 mm), one gets $a_{11} \sim 0.7$ for $C_I = 0.04$ and $a_{11} \sim 0.9$ for $C_I = 0.001$.

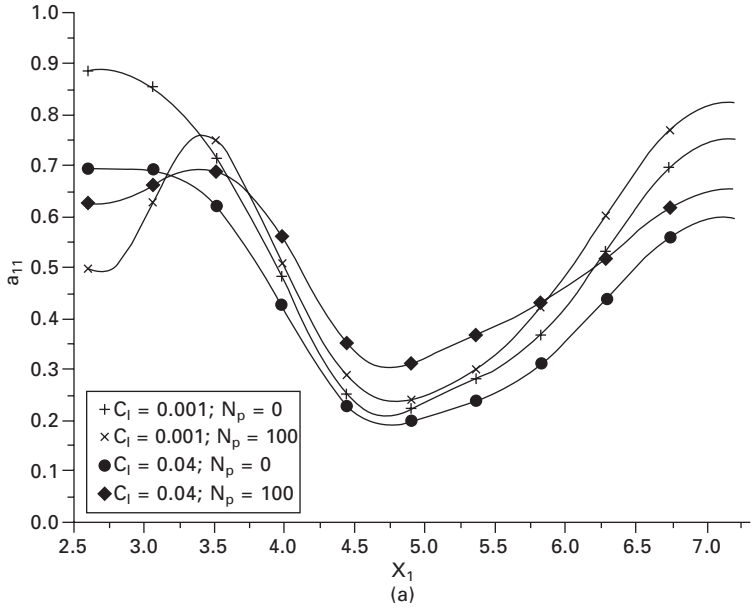

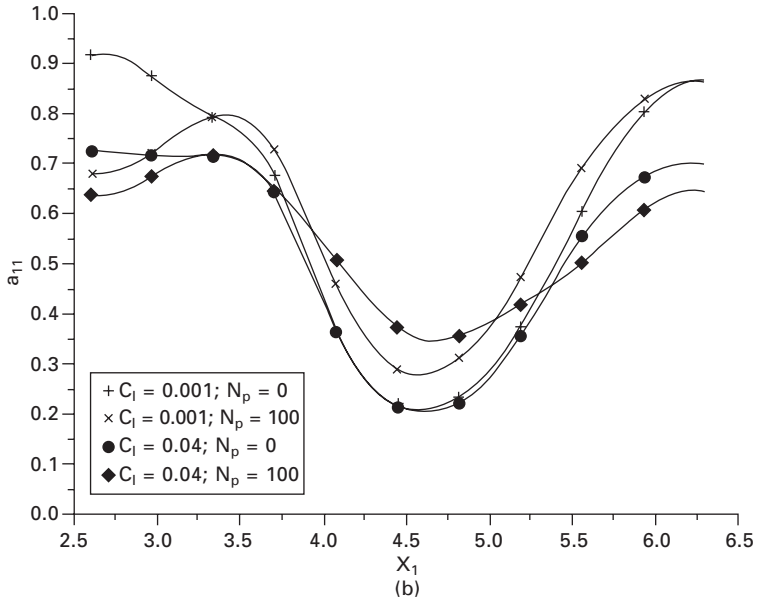

20.9 Values of orientation tensor coefficient a_{11} for the four sensors A (a), B (b), C (c), D (d) for PAA50 and isotropic initial orientation: C_l = 0.001, 0.04; N_p = 0, 100.

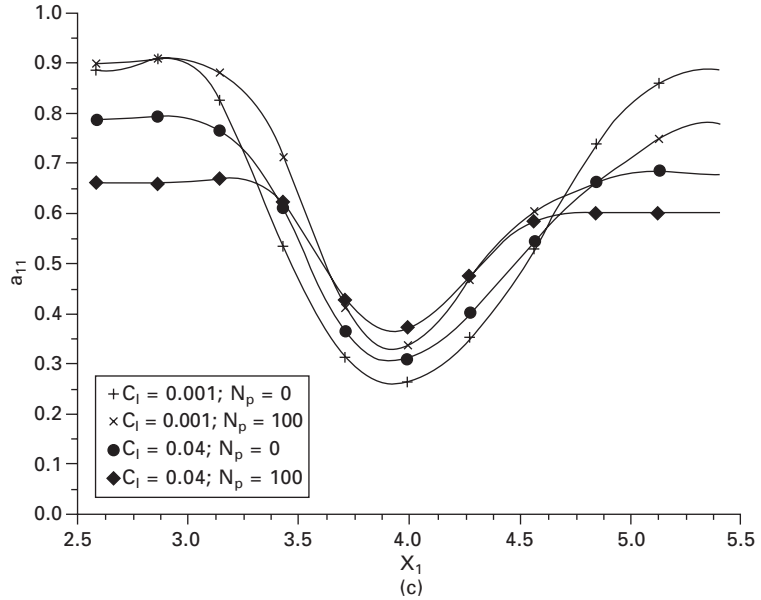

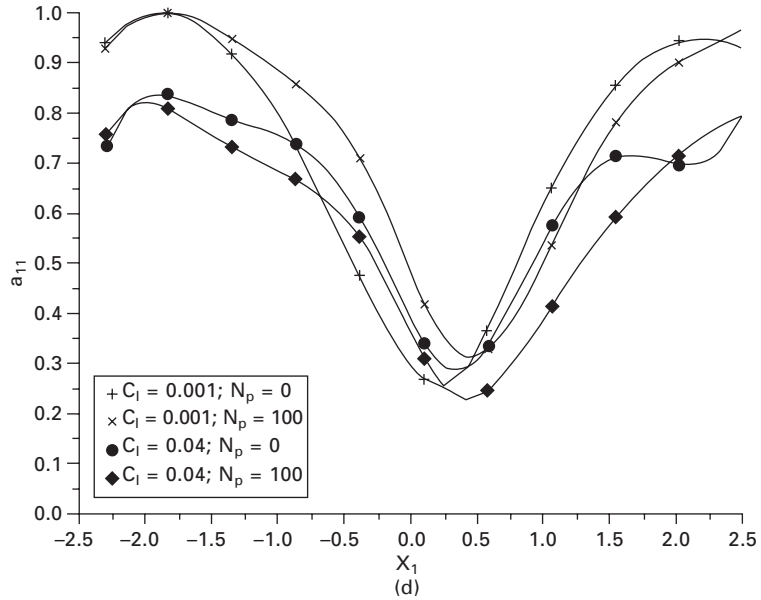

20.9 Continued.

This can be explained by the fact that shear is dominant near the walls, and it tends to orient fibres in the flow direction. The interaction term tends to disorient fibres, and its effect increases with C_I. The orientation in the core does not really change when C_I varies.

3. An increase of N_p from 0 to 100 (that is, comparison between coupled and partially coupled calculations) leads to complex tendencies in the skin regions. In the lower skin region, that is for $x_2 = 2.5$ mm, a_{11} decreases in positions A and B, but the change is negligible in positions C and D. At the opposite skin, there is no noticeable effect for positions B and D. The trends are opposite in region A (a_{11} increases) and C (a_{11} decreases), which points out the complex coupling effect on the flow velocity.
4. In the core region, taking the rheological coupling into account leads to a small increase of a_{11}, except in position D for $C_I = 0.04$. In position D, the lowest value of a_{11} is for $N_p = 100$ and $C_I = 0.04$.

Computations realised with unidirectional initial orientation (see Fig. 20.10) show that:

1. For the weakly coupled calculations ($N_p = 0$) and $C_I = 0.04$, a skin/core structure is formed as for the isotropic initial orientation. Nevertheless, the core is less oriented perpendicular to the flow direction: we get a_{11} around 0.3–0.4 for positions A, B and C, instead of 0.2–0.3. The behaviour is completely different for $C_I = 0.001$: orientation is in the flow direction on the whole thickness at positions A and B. a_{11} begins to decrease a little in the core in position C, and in D the orientation is isotropic ($a_{11} = 0.5$).
2. When N_p goes from 0 to 100, in the skin and core regions, a_{11} decreases a little, or remains nearly constant, depending on the position and the value of C_I.
3. The influence of the initial orientation is not very important in the last probe D, especially at the surfaces, except for $C_I = 0.001$ and $N_p = 0$ in the core: orientation is 2D isotropic in plane ($\boldsymbol{i}_1$, $\boldsymbol{i}_2$) for a unidirectional initial orientation ($a_{11} = 0.5$), whereas a transverse orientation is formed with an isotropic initial orientation ($a_{11} = 0.25$).

Numerical results have been compared to the experiments (Redjeb, 2007). The measured points are in between the results obtained with both initial orientation, but the agreement is better for the unidirectional initial orientation. This is not surprising, as a circular channel orients fibres mainly in the flow direction. In the skin regions, the agreement is quite good with $C_I = 0.04$ for the four locations A, B, C and D. The coupled calculation does not improve the quality of the agreement significantly. In the core region, agreement is better for $C_I = 0.001$. These results show that the interaction coefficient may depend on the orientation. However, the computed skin/core orientation at the beginning of the plaque remains more important with respect to the measurements.

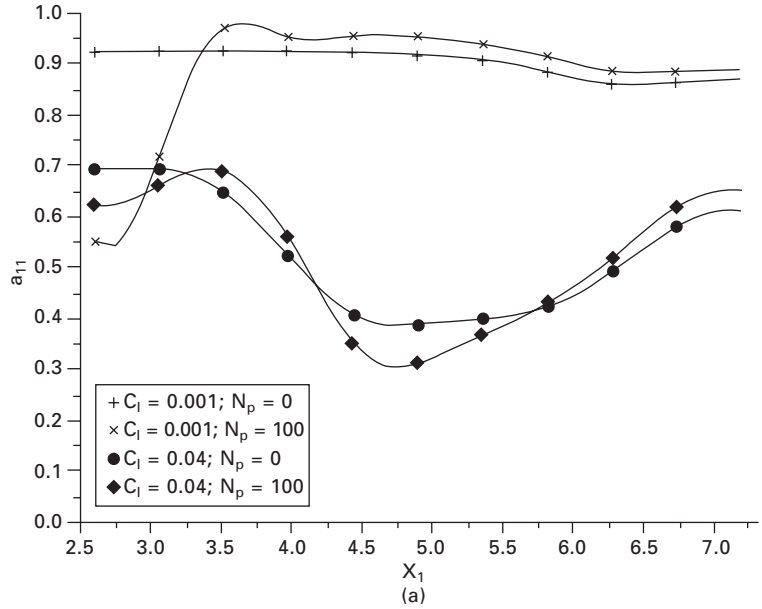

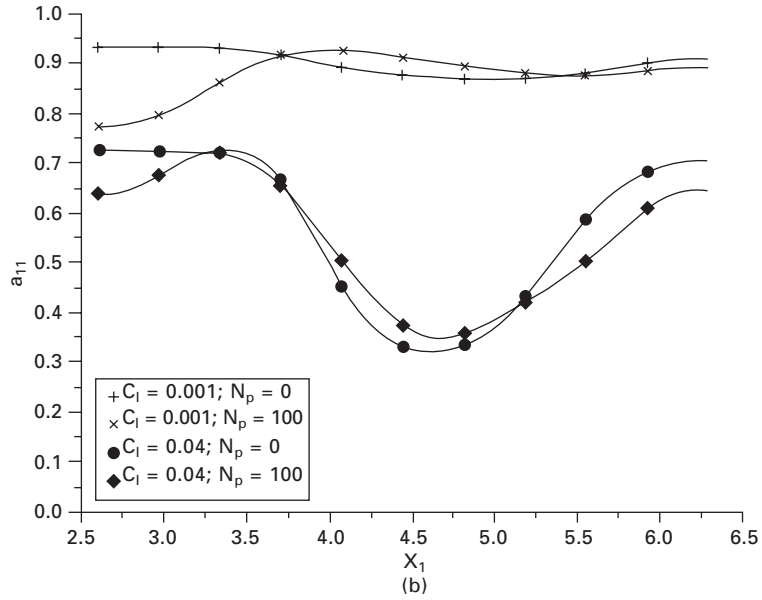

20.10 Values of orientation tensor coefficient a_{11} in the four areas A (a), B (b), C (c), D (d) for PAA50 and unidirectional initial orientation: C_I = 0.001, 0.04; N_p = 0, 100.

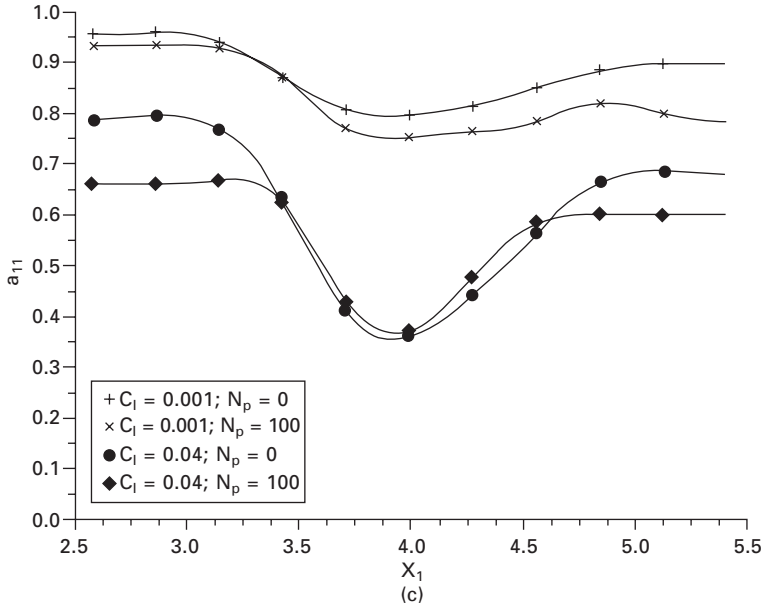

(c)

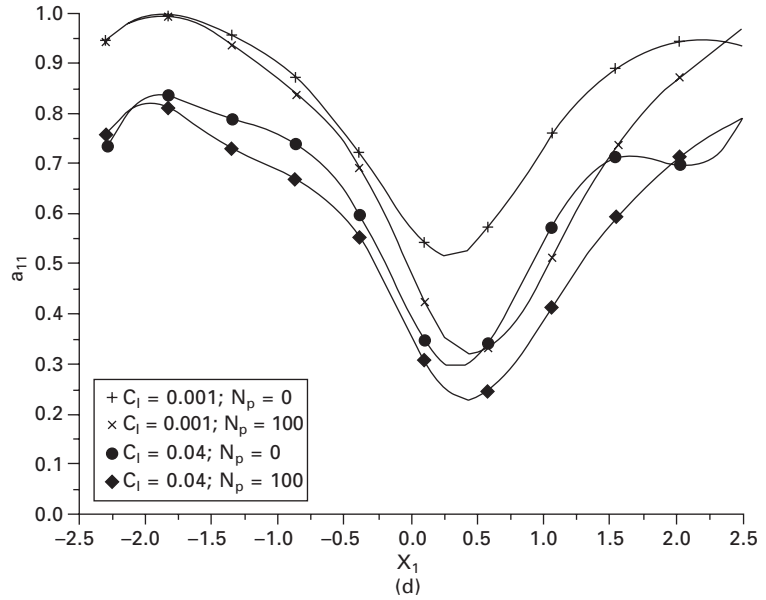

(d)

20.10 Continued.

20.4.4 U-shaped part with thin walls and cross-ribs

The studied part is presented in Fig. 20.11(a). The computations have used a mesh generated by a topologic mesher (Gruau and Coupez, 2005, or Coupez, 2010) governed by a natural metric in order to capture the thin walls. This

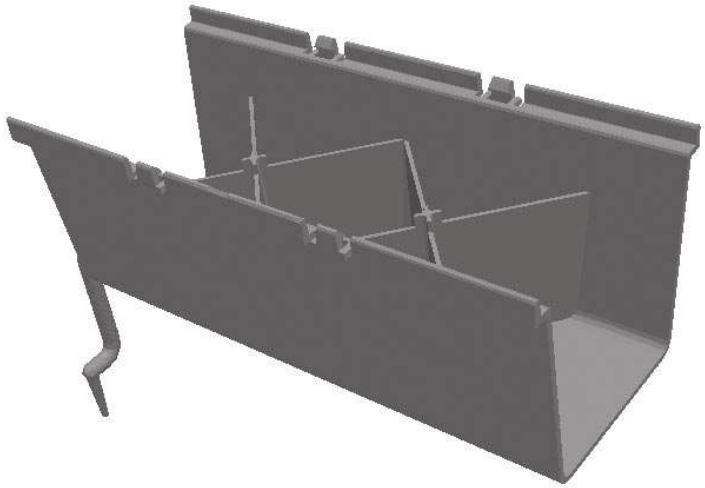

(a)

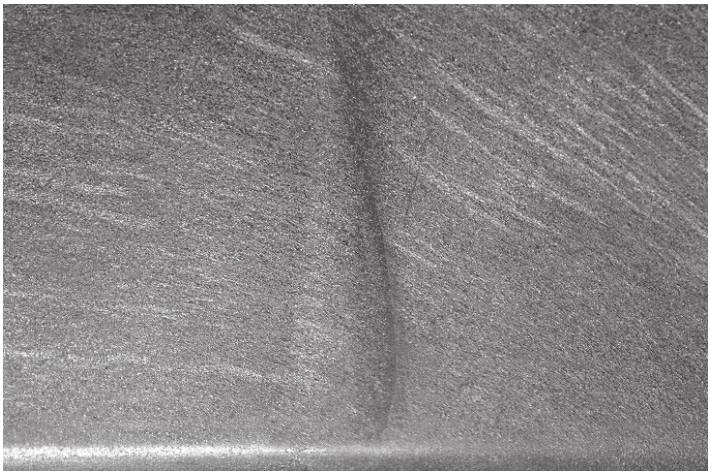

(b)

20.11 (a) Geometry of a cross with thin walls; (b) focus on the weld line located on the wall.

metric takes into account, for each area of mould, a specified mesh size in each principal direction, ensuring an appropriate number of elements in the whole thickness of the part. The injected material is a polypropylene referenced as STAMAX P30YM240. This material is modelled by a Carreau–Yasuda law for the rheology and an Arrhenius law for thermo-dependency (the parameters are given in Table 20.2). The polymer is injected at 250°C and we assume that the mould is fully regulated at 40°C. Initially, the air inside the cavity is also considered to be at a temperature of 40°C.

To compute the fibre orientation, one takes a fibre aspect ratio $\beta = 10$, an interaction coefficien $C_I = 0.001$, a hybrid closure approximation and a weakly coupling (N_s, $N_p = 0$). The orientation is analysed after a total filling time of 3.7 s. The time step is 3×10^{-4}s. The dynamics of filling are important because it helps to understand the dynamics of fibre orientation. The flow is fully symmetrical and it starts from the inlet to fill the bottom, the walls and the crossing central ribs simultaneously. In the beginning, the wall filling is slightly delayed compared to central ribs. This delay disappears and is reversed as soon as the cavity is half-filled.

The cross-ribs have two weld lines as fronts from the flank and ribs intersect twice. The first weld line is located on the sidewall after crossing the first rib. The second weld line is located at the second row of crossing ribs, as the flow front from the sidewall is faster and has time to penetrate the rib.

We focus now on the first weld line which is easily detected by the computation. Figure 20.11(b) is a photograph of the part showing the weld line. The injection gate is located at the bottom right and the presence of fibres at the surface allows seeing this line which is located in the middle of the wall. This line is slightly oriented in the direction of flow.

Tracing the isosurfaces of components of the orientation tensor (see Fig. 20.12), it is possible to find this weld line. The orientation on the side wall becomes unidirectional along the i_1 direction: a_{11} increases while a_{22} remains relatively low. At the intersection of the two fronts in the region where the ribs are connected to the wall, we can observe a decrease of component a_{11} along the entire weld line and an increase of component a_{22}. Therefore, the weld line is well located and predicted where there is a disturbance of the orientation tensor.

20.4.5 Rib-shaped part with thin walls

The studied part is presented in Fig. 20.2. It is a plaque with seven ribs and it is filled from one side. The variation of fibre concentration inside the part described in the second section is not considered in our model although it is important in terms of mechanical properties. The part has a plane of symmetry and computations are made on only half of the cavity. These computations are made for aspect ratio $\beta = 30$, $C_I = 0.023$ and N_s, $N_p = 0$. The fluid is a Stamax P40YM243 composed of a polypropylene matrix and 40% of glass fibres. The total filling time is around 1 s. Finally, computations are compared to experimental observations.

In Figs 20.13 and 20.14, the ellipsoids associated with the orientation tensor are plotted and are more or less elongated according to fibre orientation. They are also coloured by a von Mises scalar (equation 20.35) in order to give information on the anisotropy of fibre orientation. In Fig. 20.12, the skin/

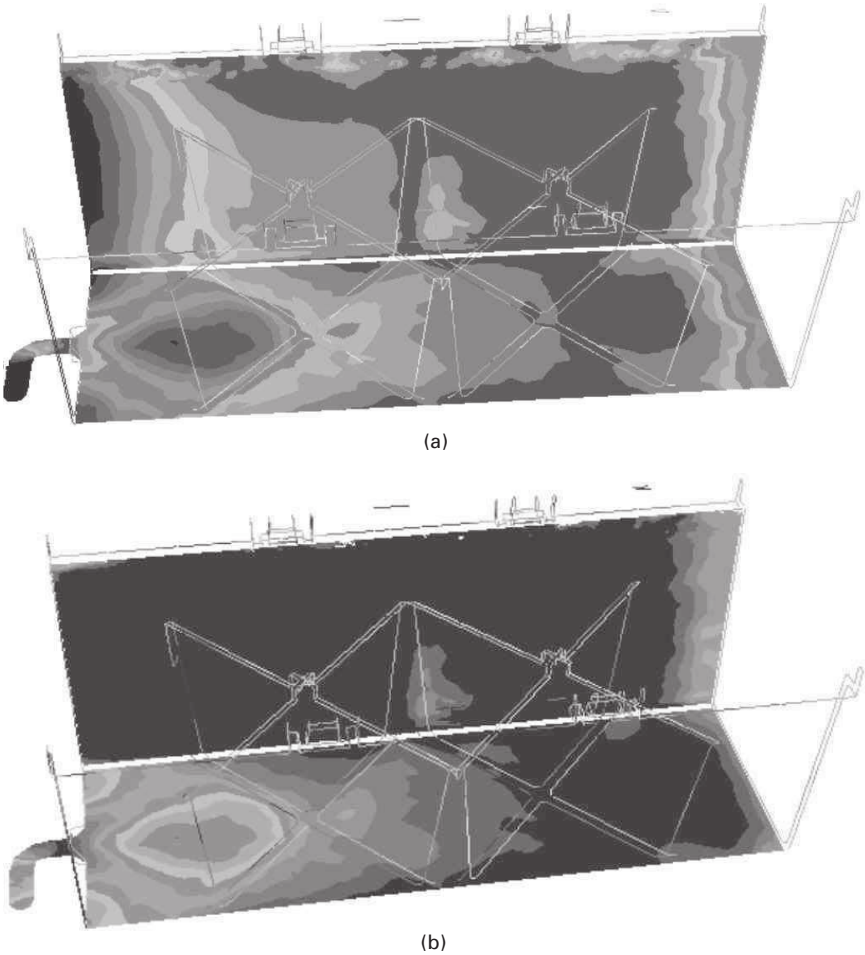

(a)

(b)

20.12 Isovalues of a_{11} and a_{22} on the wall where the weld line is located.

core phenomenon is observed in plaque as shown in experiments. However, with the Folgar and Tucker (1984) model, an isotropic orientation is obtained in the core instead of an orientation perpendicular to the flow motion in the experiment. In the skin region, the orientation along the flow motion is observed in both experiments and computations.

For the ribs, the orientation changes during filling: first during rib filling, a core/skin orientation is observed; secondly, there is a 'disorientation' of fibres once the rib is filled. Finally, only the base of the rib maintains a non-isotropic orientation.

In Fig. 20.13, we compare the simulation with the experimental observation when the mould is fully filled (the experimental picture is slightly larger than

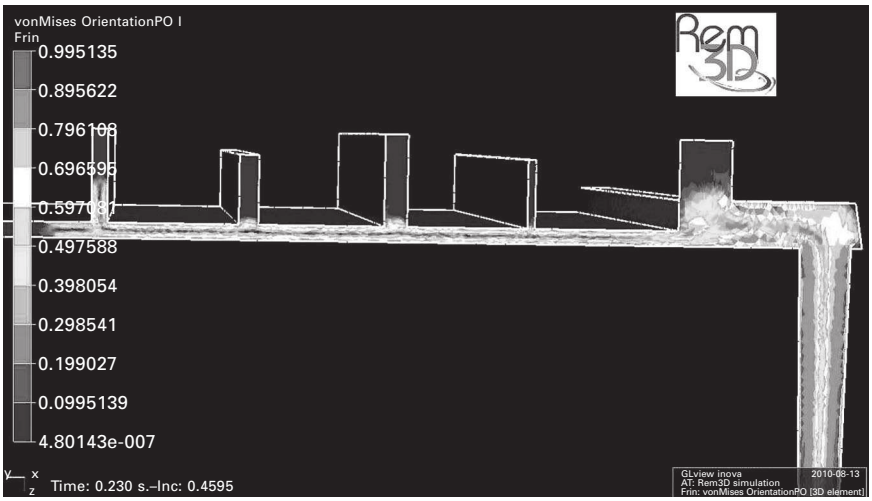

20.13 Ellipsoids representing orientation tensor coloured by von Mises scalar for the plaque with ribs: isotropic orientation (white), unidirectional orientation (black).

the image obtained by the simulation). We deduce that the simulation allows reproducing the increase of the thickness of the core area at the base of the ribs. Moreover, the numerical model reproduces the arch drawn orientation. As in experimental observations, a homogeneous orientation is recovered inside the rib. However, this orientation is isotropic in simulations, whereas the fibres are oriented in a direction parallel to the rib in experiments. Moreover, the arch orientation depends on the time of packing, which was not taken into account in our simulations.

Finally, Rem3D software recovers reasonably faithfully the orientation encountered in the experiments. Only the areas having an isotropic orientation are not in agreement with the experiments. To overcome this discrepancy, a tensorial interaction coefficient C_I has to be introduced as prescribed by anisotropic rotary diffusive models. In this way, the anisotropy of the plaque will be taken into account (the vertical direction is smaller with respect to the two others).

20.5 Conclusions

Fibre structure in reinforced moulded components is directly related to the process. Fibre length degradation takes place mostly in the plasticising unit but the fibre length distribution is not yet considered in our modelling. Fibre concentration can be considered as constant to a first approximation even though, in the plaque with ribs, we measured some important fluctuations inside the part. Therefore the evolution of fibre concentration may have

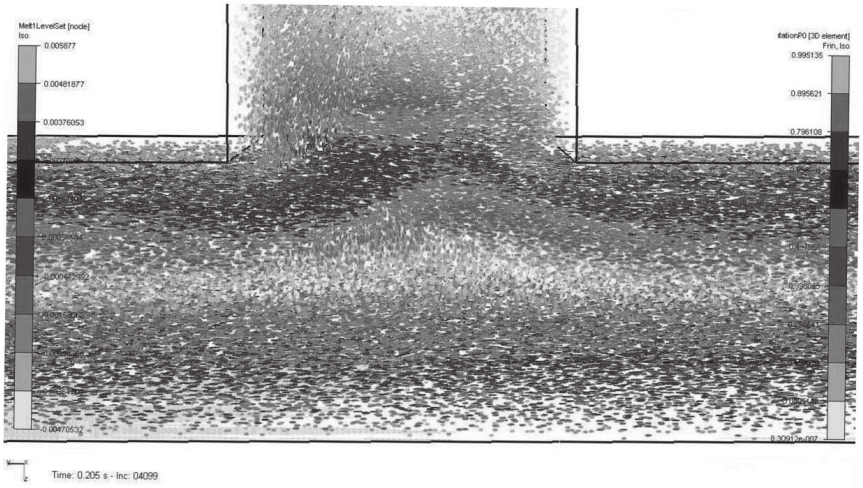

(a)

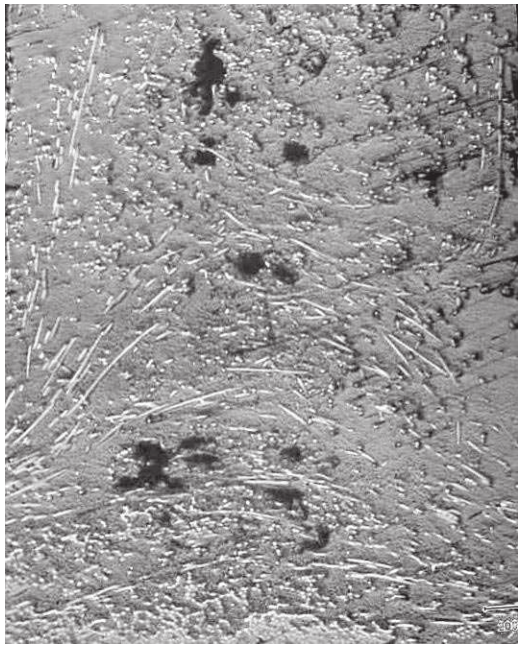

(b)

20.14 (a) Final arch drawn orientation near the third rib; (b) comparison with the experiment.

an influence on the evolution of fibre orientation during the process. Fibre orientation varies a lot throughout the part, especially in the thickness. A core region with fibres transverse to the flow direction is almost always created

in the gate region, because of high elongation rates. Near the surfaces, fibres are predominantly oriented in the flow direction.

Quantification of fibre orientation is time consuming, with several causes of errors. Modelling of flow-induced fibre orientation is usually carried out supposing an equivalent viscous behaviour for the composite. This gives valuable information for mould design, and especially gate location. The closure approximation has a larger influence on the results than does the interaction coefficient. Full 3D computations give a precise kinematics description in the gate, at the flow front, which increases the precision of the orientation calculation. Coupling between rheology and orientation becomes important, raising the issue of the validity of constitutive equations based on dilute or semi-dilute Newtonian suspension, and of the determination of rheological parameters. The numerical computations describe reasonably well the orientation encountered in the experiments. The discrepancy could be overcome by making the model more complex, but the number of parameters increases and there is no simple way to get them. Then, both the experimental setup and numerical procedures (inverse analysis) have to be developed to identify these parameters for the polymers used in industrial processes.

20.6 References and further reading

Advani S G, Tucker C L (1987), 'The use of tensors to describe and predict fiber orientation in short fiber composites', *J Rheol*, 31, 751–784.

Advani S G, Tucker C L (1990), 'Closure approximations for three-dimensional structure tensors', *J Rheol*, 34, 367–386.

Akay M, Barkley D (1991), 'Fiber orientation and mechanical behavior in reinforced thermoplastic injection moldings', *J Mater Sci*, 26, 2731–2742.

Akay M, O'Regan D F, Bailey R S (1995), 'A model to predict the through-thickness distribution of heat generation in cross-ply carbon-fiber composites', *Comp Sci Technol*, 55, 109–118.

Altan M C, Selcuk S S, Guceri I, Pipes R B (1990), 'Numerical prediction of three-dimensional fiber orientation in hele-shaw flows', *Polym Eng Sci*, 30, 848–859.

Arroyo M, Avalos F (1989), 'Polypropylene/low density polyethylene blend matrices and short glass fibers based composites. I. Mechanical degradation of fibers as a function of processing method', *Polym Comp*, 10(2), 117–121.

Avérous L, Quantin J C, Crespy A, Lafon D (1997), 'Evolution of the three-dimensional orientation of glass fibers in injected isotactic polypropylene', *Polym Eng Sci*, 37(2), 329–337.

Batchelor G K (1970), 'Slender body theory for particles arbitrary cross section in Stokes flow', *J Fluid Mech*, 44, 419–440.

Batchelor G K (1971), 'The stress generated in a non dilute suspension of elongated particles by pure straining motion', *J Fluid Mech*, 46, 813–829.

Batkam S, Bruchon J, Coupez T (2004), 'A space-time discontinuous Galerkin method for convection and diffusion in injection moulding', *Int J Forming Processes*, 7, 11–33.

Bay R S, Tucker III C L (1992), 'Stereological measurement and error estimates for three-dimensional fiber orientation', *Polym Eng Sci*, 32(4), 240–253.

Beaume G (2009), 'Modelling and numerical simulation of a complex fluid flow', PhD thesis ENSMP, http://tel.archives-ouvertes.fr/tel-00416435/fr/

Bretherton F P (1962), 'The motion of rigid particles in a shear flow at low Reynolds number', *J Fluid Mech*, 14, 284–304.

Chin W, Liu H, Lee Y (1988), 'Effects of fiber length and orientation distribution on the elastic modulus of short fiber reinforced thermoplastics', *Polym Comp*, 9(1), 27–35.

Cintra J, Tucker C L (1995), 'Orthotropic closure approximation for flow induced fiber orientation', *J Rheol*, 34, 1095–1122.

Clarke A, Eberhardt C (2002), *Microscopy Techniques for Materials Science*, Woodhead Publishing, Cambridge, UK.

Coupez T (2010), 'Metric construction by length distribution tensor and edge based error for anisotropic adaptive meshing', *J Comp Phys*, doi:10.1016/j.jcp.2010.11.041.

Davidson N C, Clarke A R (1999), 'Extending the dynamic range of fibre length and fibre aspect ratios by automated image analysis', *J Microsc*, 196, 266–272.

Denault T, Vu-Khanh T, Foster B (1989), 'Tensile properties of injection molded long fiber thermoplastic composites', *Polym Comp*, 10, 313–321.

Dinh S, Armstrong R (1984), 'A rheological equation of state for semiconcentrated fibre suspensions', *J Rheol*, 28, 207–227.

Dontula N, Ramesh N S, Campbell G A, Small J D, Fricke A L (1994), 'An experimental study of polymer–filler redistribution in injection molded parts', *J Reinf Plast Comp*, 13, 98–110.

Dupret F, Verleye V (1998), 'Modeling the flow of fiber suspensions in narrow gaps', in *Advances in the Flow and Rheology of Non-Newtorian Fluids*, Siginer D A, De Kee D, Chhabra R P (eds), Elsevier, Amsterdam, 1347–1398.

Eberhardt C, Clarke A R (2001), 'Fibre orientation measurements in short glass fibre composites; I, Automated, high angular resolution measurement by confocal microscopy', *Comp Sci Tech*, 61, 1389–1400.

Eriksson P A, Albertsson A C, Boydell P, Prautzsch G, Månson J A (1996), 'Prediction of mechanical properties of recycled fiberglass reinforced polyamide 66', *Polym Comp*, 17(6), 830–839.

Fan X, Phan-Thien N, Zheng R (1998), 'A direct simulation of fibre suspensions', *J Non-Newtonian Fluid Mech*, 74, 113–135.

Férec J, Ausias G, Heuzey M C, Carreau P J (2009), 'Modeling fibre interactions in semi-concentrated fibre suspensions', *J Rheol*, 53, 49–72.

Folgar F, Tucker C L (1984), 'Orientation behavior of fibers in concentrated suspensions', *J Reinf Plast Comp*, 3, 98–119.

Franzen B, Klason C, Kubat J, Kitano T (1989), 'Fibre degradation during processing of short fibre reinforced thermoplastics', *Composites*, 20(1), 65–76.

Gruau C, Coupez T (2005), '3D tetrahedral, unstructured and anisotropic mesh generation with adaptation to natural and multidomain metric', *Comp Meth Appl Mech Eng*, 194, 4951–4976.

Gupta V B, Mittal R K, Sharma P K, Menning G, Wolters J (1989), 'Some studies on glass fibre-reinforced polypropylene. Part II: Mechanical properties and their dependence on fiber length, interfacial adhesion and fiber dispersion', *Polym Comp*, 10(1), 8–15.

Hand G (1961), 'A theory of dilute suspension', *Arch Rat Mech Anal*, 7, 81–86.

Hegler R P, Menning G (1985), 'Phase separation effects in the processing of glass bead and glass fiber filled thermoplastics by injection molding', *Polym Eng Sci*, 25, 395–405.

Hinch E, Leal L (1973), 'Time dependent shear flows of a suspension of particles with weak Brownian rotations', *J Fluid Mech*, 57, 753–767.

Jeffery G B (1922), 'A theory of anisotropic fluids', *Proc Roy Soc London*, A102, 161–179.

Kabanémi K K, Hétu J F (1999), 'Modelling and simulation of nonisothermal effects in injection moulding of rigid fibres suspensions', *J Inj Molding Technol*, 3, 80–87.

Kamal M R, Song L, Singh P (1986), 'Measurement of fibre and matrix orientations in fibre reinforced composites', *Polym Comp*, 7(5), 323–832.

Koch D L (1995), 'A model for orientational diffusion in fiber suspensions', *Phys Fluids*, 7, 2086–2088.

Kubat J, Szalanczi A (1974), 'Polymer–glass separation in the spiral mold test', *Polym Eng Sci*, 14, 873–877.

Lipscomb G G, Keunigs R, Marucci G, Denn M M (1984), 'A continuum theory for fiber suspensions', *Proc. IX Int. Congress on Rheology*, 2, 497–503.

Lipscomb G, Denn G, Hur M, Hur D, Boger D (1988), 'The flow of fibre suspensions in complex geometries', *J Non-Newtonian Fluid Mech*, 26, 297–325.

Martinéz M A, Cueto E, Doblaré M, Chinesta F (2003), 'Natural element meshless simulation of flows involving short fiber suspensions', *J Non-Newtonian Fluid Mech*, 115, 51–78.

Miled H, Silva L, Agassant J-F, Coupez T (2008), 'Numerical simulation of fiber orientation and resulting thermo-elastic behaviour in reinforced thermoplastics', in *Mechanical Response of Composites*, Camanho P (ed.), Springer, Berlin.

Moses K B, Advani S G, Reinhardt A (2001), 'Investigation of fiber motion near solid boundaries in simple shear flow', *Rheol Acta*, 47, 63–73.

Papathanasiou T D (1997), 'Flow-induced alignment in injection molding of fiber-reinforced polymer composites', in *Flow-induced Alignment in Composite Materials*, Papathanasiou T D and Guell D C (eds), Woodhead Publishing, Cambridge, UK, 112–165.

Phan-Thien N, Fan X J, Tanner R I, Zheng R (2002), 'Folgar–Tucker constant for a fibre suspension in a Newtonian fluid', *J Non-Newtonian Fluid Mech*, 103, 251–260.

Phelps J H, Tucker C L (2009), 'An anisotropic rotary diffusion model for fiber orientation in short- and long-fiber thermoplastics', *J Non-Newtonian Fluid Mech*, 156, 165–176.

Pichelin E, Coupez T (1998), 'Finite element solution of the 3D mould filling problem for viscous incompressible fluid', *Comp Meth Appl Mech Eng*, 163, 359–371.

Pichelin E, Coupez T (1999), 'A Taylor discontinuous Galerkin method for the thermal solution in 3D mould filling', *Comp Meth Appl Mech Eng*, 178, 153–169.

Prager S (1957), 'Stress–strain relation in a suspension of dumbbells', *J Rheol*, 1, 53–62.

Ranganathan S, Advani S G (1991), 'On modeling fiber–fiber interactions of flowing suspensions in homogeneous flows', *J Rheol*, 35, 1499–1522.

Redjeb A (2007), 'Numerical simulation of fibre orientation in injection of reinforced thermoplastics', PhD thesis ENSMP, http://tel.archives-ouvertes.fr/tel-00332719/fr/

Redjeb A, Silva L, Laure P, Vincent M, Coupez T (2005), 'Numerical simulation of fibre orientation in injection moulding process', *21st International Polymer Processing Society Meeting*, Leipzig, Germany.

Shaqfeh E, Fredrickson G (1990), 'The hydrodynamic stress in a suspension of rods', *Phys Fluids A*, 2, 7–24.

Shen H B, Nutt S, Hull D (2004), 'Direct observation and measurement of fiber architecture in short fiber–polymer composite foam through micro-CT imaging', *Comp Sci Technol*, 64, 2113–2120.

Tremblay S R, Lafleur P G, Ait-Kadi A (2000), 'Effects of injection parameters on fiber attrition and mechanical properties of polystyrene molded parts', *J. Inj. Molding Technol*, 4(1), 1–7.

Tucker C L (1991), 'Flow regimes for fiber suspensions in narrow gap', *J Non-Newtonian Fluid Mech*, 39, 239–268.

Ville L, Silva L, Coupez T (2010), 'Convected level set method for the numerical simulation of fluid buckling', *Int J Num Meth Fluids*, doi:10.1002/fld.2259.

Vincent M, Giroud T, Clarke A, Eberhardt C (2005), 'Description and modeling of fiber orientation in injection molding of fiber reinforced thermoplastics', *Polymer*, 46, 6719–6725.

Vincent M (2009), 'Flow induced fiber micro-structure in injection molding of fiber reinforced materials', in *Injection Molding, Technology and Fundamentals*, Kamal M R, Isayev A I, Liu S J (Eds), Carl Hanser Verlag, Munich 253–272.

Wang J, O'Gara J F, Tucker C L (2008), 'An objective model for slow orientation kinetics in concentrated fiber suspensions: Theory and rheological evidence', *J Rheol*, 52, 1179–1200.

Wetzel E D, Tucker C L (1999), 'Area tensors for modeling microstructure during laminar liquid–liquid mixing', *Int J Multiphase Flow*, 25, 35–61.

Yamane Y, Kaneda Y, Dio M (1994), 'Numerical simulation of semi-dilute suspensions of rodlike particles in shear flow', *J Non-Newtonian Fluid Mech*, 54, 405–421.

21
Modelling composite reinforcement forming processes

P. BOISSE and N. HAMILA, Université de Lyon, France

Abstract: In this chapter various finite element approaches for the simulation of woven reinforcement forming are presented. Some are based on continuous modelling, while others, known as discrete or mesoscopic approaches, model each yarn of the fabric. The intermediary semi-discrete approach is also examined. During this approach the shell finite element interpolation formula maintains the continuity of the displacement field, but the internal virtual work is obtained as the sum of tension, in-plane shear and bending cells, of all the woven unit cells within the element. When using continuous approaches, the necessity of taking the strong specificity of the fibrous material into account causes difficulties. The main goal of the hypoelastic and hyperelastic constitutive models presented in this chapter is to describe this specific mechanical behaviour. During discrete and semi-discrete approaches the directions of the yarns are 'naturally' followed because the yarns themselves are modelled. The advantages and drawbacks of the different approaches are also discussed.

Key words: fabric, textiles, preforming, draping, meso/macroscopic approaches, hypoelasticity, hyperelasticity.

21.1 Introduction

Textile composites offer a number of attractive properties; they possess a high capacity to conform to complicated contours, they are suitable for manufacturing components with complex shapes, and they offer a greater flexibility in processing options compared to metals and even to their non-woven counterparts. A double curved composite preform shape can be accomplished through the forming of an initially flat fibrous reinforcement. This reinforcement can be dry (i.e. without resin) such as in the preforming stage of liquid composite moulding (LCM) processes (Advani, 1994; Parnas, 2000). These processes, especially the resin transfer moulding (RTM) process, can be used to manufacture highly loaded composite parts for aeronautical applications such as helicopter frames (Dumont *et al.*, 2008) and motor blades (de Luycker *et al.*, 2009). During these LCM processes the resin is injected into a preform which can be doubly curved such as those shown in Fig. 21.1 (Woven Composites Benchmark Forum, 2004) and Fig. 21.2 (European project ITOOL (ITOOL, Allaoui *et al.*, 2011)). In the case of thermoset or

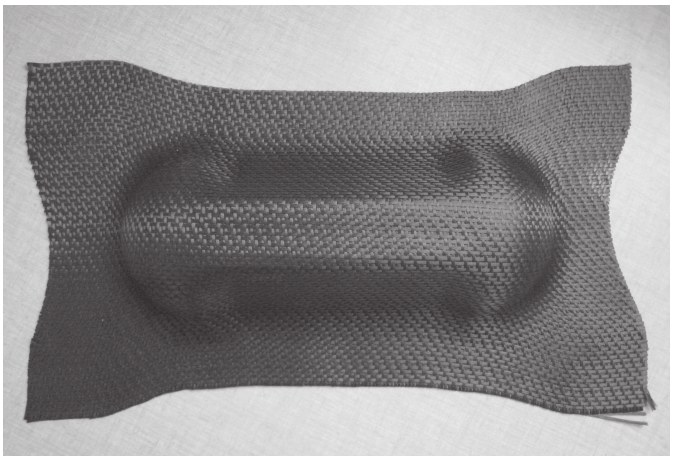

21.1 Preform analysed in the double dome international benchmark.

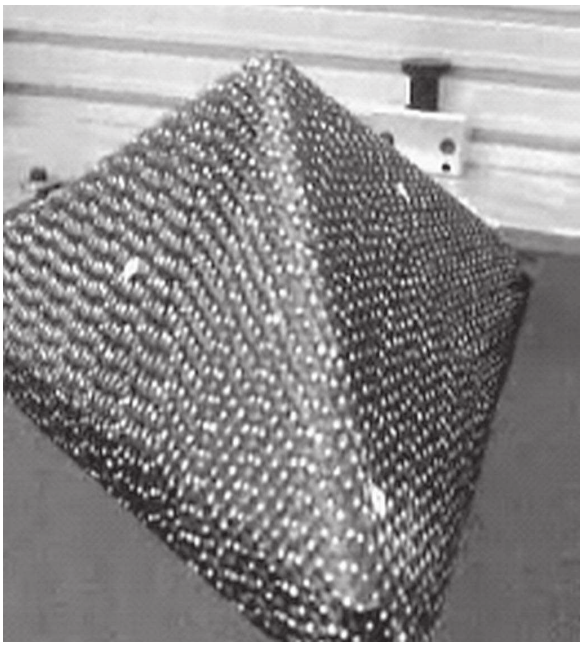

21.2 Tetrahedral shape form.

thermoplastic prepregs, the resin is present within the reinforcement during the forming stage, but exists in a weak state. In thermoset prepregs this is because the resin it is not yet polymerized, and in thermoplastic prepregs it

is because the process is performed at a high temperature. The resin is not hardened and the forming is mainly led by the reinforcement. The in-plane shear strain of the woven reinforcements can be very high during the forming of double-curved parts. The orientation and density of fibres in the deformed shape directly influences the permeability of reinforcement and becomes crucial in predicting the mechanical behaviour of the final part (Hammami *et al.*, 1996; Loix *et al.*, 2008). The yarns are made up of several thousands of fibres and their mechanical behaviour is very singular and specific. In order to develop the composite forming simulation codes, therefore, large deformations of the textile reinforcements are subject to a sustained effort to simulate and model them.

The approach chosen to model the forming of textile composite reinforcements depends on the scale at which the analysis is made. The analysis of the deformation can be made by considering and modelling each of its yarns (or fibres) and their interactions such as contact with friction. Approaches made using this level of analysis are called discrete or mesoscopic. The disadvantage of these approaches is that the number of yarns (and even more so the number of fibres) is high and the interactions are complex. The alternative continuous approaches consider a continuous medium juxtaposed with the fabric, the mechanical behaviour of which is equivalent to those of the textile reinforcement. The disadvantage of using continuous approaches is that this mechanical behaviour is complex. It concerns large strains and strong anisotropy and evolves a great deal during the forming. Throughout this chapter continuous and discrete approaches for composite reinforcements forming simulations will be introduced. First a mesoscopic approach during which each yarn of a woven cell is modelled with shell elements with contact and friction is presented, followed by two continuous approaches based respectively on a hyperelastic and a hypoelastic model. Finally a semi-discrete approach, which is an intermediate method between the continuous and discrete approaches, is presented. The advantages and drawbacks of the different approaches are also discussed.

21.2 A mesoscopic approach

In mesoscopic approaches, the modelling measures each fibre bundle (yarn). This approach can also be described as a discrete approach since there are a discrete number of yarns in the preform. The modelling of each yarn must be simple enough to render the simulation of the whole reinforcement forming possible. The interactions between warp and weft directions are precisely taken into account by considering the contact and friction caused by relative motions between the yarns (Pickett *et al.*, 2005; Duhovic and Bhattacharyya, 2006). This modelling could be performed at the microscopic level, i.e. by considering each fibre as a beam. Nevertheless, the massive number of fibres

per yarn (some thousands in the case of composite reinforcements), and therefore the huge amount of contacts with friction which have to be taken into account, lead to a very costly computation. For this reason, although this approach is promising, only very small elements of the fabric have been modelled to date (Durville, 2005; Miao *et al.*, 2008). The mesoscopic approach considers the continuous behaviour of each yarn. This continuous behaviour must take the fibrous nature of the yarn into account in order to ensure that rigidities in bending and transverse compression remain very small in comparison to the tensile stiffness. The modelling of the woven unit cell must be as accurate as possible but simple enough to allow the computation of the forming process of the entire reinforcement.

Figure 21.3(a) shows the finite element model used for discrete simulations of forming processes (216 degrees of freedom (DOF)). It is compared to another FE model of the unit cell used in Badel *et al.* (2008) (Fig. 21.3(b))

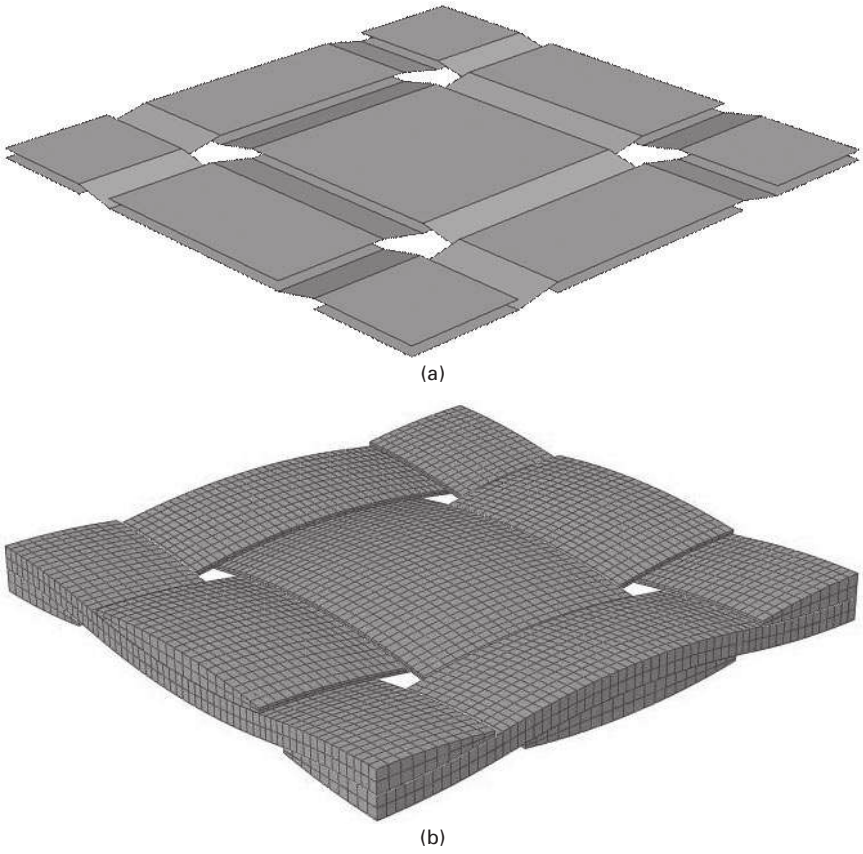

21.3 Modelling of a unit cell of a plain weave at the mesoscopic level: (a) 216 dof FE model; (b) 47214 dof FE model.

to analyse the local in-plane shear of a plain weave unit cell (47214 DOF). A simulation of the forming of a composite reinforcement can be based on the model of Fig. 21.3(a), but not on those of Fig. 21.3(b) because of the computational cost. In the simplified unit cell (Fig. 21.3(a)) each yarn is described by few shell elements and the contact friction and possible relative displacement of the yarns are considered. The bending stiffness of the yarns is independent of the tensile rigidity and very much reduced in comparison to the results given by plate theories. The membrane behaviour is based on a hypoelastic model. A stress rate $\underline{\underline{\boldsymbol{\sigma}}}^{\nabla}$ is related to the strain rate $\underline{\underline{\mathbf{D}}}$ by a constitutive tensor $\underline{\underline{\underline{\underline{\mathbf{C}}}}}$. To avoid rigid body rotations which can affect the stress state, the derivative $\underline{\underline{\boldsymbol{\sigma}}}^{\nabla}$, called the objective derivative, is the derivative for an observer who is fixed with respect to the material. Because this requirement is not uniquely defined there are several objective derivatives. This objective derivative is often based on a rotation $\underline{\underline{\mathbf{Q}}}$ characterizing the rotation of the material.

The rate constitutive equation (or hypoelastic law) has the form:

$$\underline{\underline{\boldsymbol{\sigma}}}^{\nabla} = \underline{\underline{\underline{\underline{\mathbf{C}}}}} : \underline{\underline{\mathbf{D}}} \tag{21.1}$$

with

$$\underline{\underline{\boldsymbol{\sigma}}}^{\nabla} = \underline{\underline{\mathbf{Q}}} \cdot \left(\frac{\mathrm{d}}{\mathrm{d}t} \left(\underline{\underline{\mathbf{Q}}}^{\mathrm{T}} \cdot \underline{\underline{\boldsymbol{\sigma}}} \cdot \underline{\underline{\mathbf{Q}}} \right) \right) \cdot \underline{\underline{\mathbf{Q}}}^{\mathrm{T}} = \dot{\underline{\underline{\boldsymbol{\sigma}}}} + \underline{\underline{\boldsymbol{\sigma}}} \cdot \underline{\underline{\boldsymbol{\Omega}}} - \underline{\underline{\boldsymbol{\Omega}}} \cdot \underline{\underline{\boldsymbol{\sigma}}} \tag{21.2}$$

and $\underline{\underline{\boldsymbol{\Omega}}}$ is the spin corresponding to $\underline{\underline{\mathbf{Q}}}$, i.e. $\underline{\underline{\boldsymbol{\Omega}}} = \dot{\underline{\underline{\mathbf{Q}}}} \cdot \underline{\underline{\mathbf{Q}}}^{T}$.

It has been shown (Badel *et al.*, 2008) that the rotation $\underline{\underline{\mathbf{Q}}}$ must be the rotation of the fibre $\underline{\underline{\boldsymbol{\Phi}}}$ in the case of fibrous materials. This is specific to fibrous materials and differs from common objective derivatives such as Green–Naghdi (Green and Naghdi, 1965) and Jaumann (Dafalias, 1983).

The current fibre direction can be determined from the gradient tensor $\underline{\underline{\mathbf{F}}}$. Assuming that the initial position of the fibre is $\underline{\mathbf{f}}_1^0 = \underline{\mathbf{e}}_1^0$:

$$\underline{\mathbf{f}}_1 = \frac{\underline{\underline{\mathbf{F}}} \cdot \underline{\mathbf{e}}_1^0}{\left\| \underline{\underline{\mathbf{F}}} \cdot \underline{\mathbf{e}}_1^0 \right\|} \tag{21.3}$$

The other basis vectors $\underline{\mathbf{f}}_2$ and $\underline{\mathbf{f}}_3$ of the orthonormal frame $\{\underline{\mathbf{f}}_i\}$ are obtained from the material transformation of $\underline{\mathbf{e}}_2^0$:

$$\underline{\mathbf{f}}_2 = \frac{\underline{\underline{\mathbf{F}}} \cdot \underline{\mathbf{e}}_2^0 - (\underline{\underline{\mathbf{F}}} \cdot \underline{\mathbf{e}}_2^0 \cdot \underline{\mathbf{f}}_1)\underline{\mathbf{f}}_1}{\left\| \underline{\underline{\mathbf{F}}} \cdot \underline{\mathbf{e}}_2^0 - (\underline{\underline{\mathbf{F}}} \cdot \underline{\mathbf{e}}_2^0 \cdot \underline{\mathbf{f}}_1)\underline{\mathbf{f}}_1 \right\|}, \; \underline{\mathbf{f}}_3 = \underline{\mathbf{f}}_1 \times \underline{\mathbf{f}}_2, \; \underline{\underline{\boldsymbol{\Phi}}} = \underline{\mathbf{f}}_i \otimes \underline{\mathbf{e}}_i^0 \tag{21.4}$$

The transverse properties of the shell are identified through a picture frame test (Gatouillat, 2010). Figure 21.4 shows the results of a hemispherical

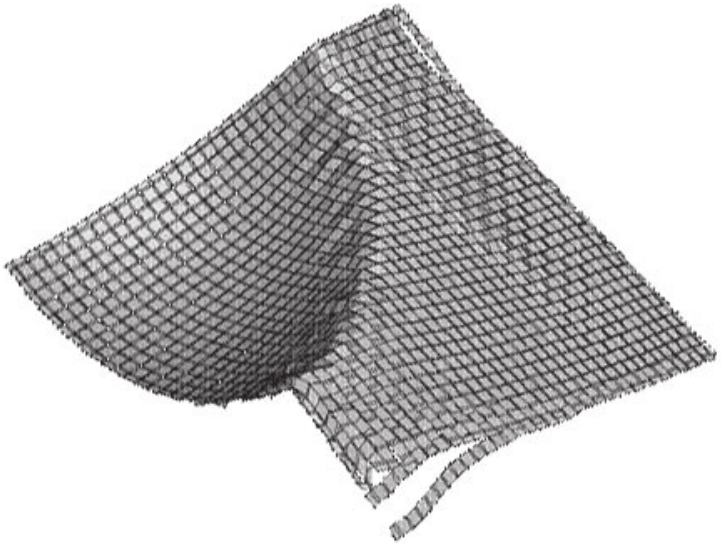

21.4 Simulation of a hemispherical forming using the unit cell model of Fig. 21.3(a).

forming simulation based on the modelling of the unit woven shell shown in Fig. 21.3(a). This meso modelling has been used in Gatouillat (2010) for the simulation of a 'double dome' benchmark (Woven Composites Benchmark Forum, 2004) and to form simulations where the continuity of the textile reinforcement is no longer ensured because of strong loads on the blank holders.

21.3 Continuous approaches

Continuous approaches consider the fibrous material as a continuum in average at the macroscopic scale. The purpose is to make use of the standard finite element codes for the analysis of fibrous media (Spencer, 2000; Peng and Cao, 2005; ten Thije *et al.*, 2007). The formulations employed within a commercial code, i.e. ABAQUS/Explicit, for stress calculations are presented comprehensively in the following. The algorithm adopted and the formulations used within a user material subroutine VUMAT are then shown.

21.3.1 Hypoelastic model

The equations governing the mechanical behaviour are given in equations 21.1–21.4. They use the rotation $\underline{\underline{\mathbf{\Phi}}}$ of the fibre. A membrane assumption is used. The Green–Naghdi's frame (GN) is the default work basis of ABAQUS/

Explicit. Its unit vectors ($\underline{\mathbf{e}}_1$, $\underline{\mathbf{e}}_2$) in the current configuration are updated from the initial orientation axes, ($\underline{\mathbf{e}}_1^0$, $\underline{\mathbf{e}}_2^0$), using the proper rotation $\underline{\underline{\mathbf{R}}}$:

$$\underline{\mathbf{e}}_1 = \underline{\underline{\mathbf{R}}} \cdot \underline{\mathbf{e}}_1^0, \quad \underline{\mathbf{e}}_1 = \underline{\underline{\mathbf{R}}} \cdot \underline{\mathbf{e}}_2^0 \tag{21.5}$$

In the current configuration, the unit vectors in the warp and weft fibre directions are respectively:

$$\underline{\mathbf{f}}_1 = \frac{\underline{\underline{\mathbf{F}}} \cdot \underline{\mathbf{f}}_1^0}{\left\| \underline{\underline{\mathbf{F}}} \cdot \underline{\mathbf{f}}_1^0 \right\|}, \quad \underline{\mathbf{f}}_2 = \frac{\underline{\underline{\mathbf{F}}} \cdot \underline{\mathbf{f}}_2^0}{\left\| \underline{\underline{\mathbf{F}}} \cdot \underline{\mathbf{f}}_2^0 \right\|} \tag{21.6}$$

($\underline{\mathbf{e}}_1^0$, $\underline{\mathbf{e}}_2^0$) and ($\underline{\mathbf{f}}_1^0$, $\underline{\mathbf{f}}_2^0$) are assumed to coincide initially (Fig. 21.5). Two orthonormal frames based on the two fibre directions are defined: g($\underline{\mathbf{g}}_1$, $\underline{\mathbf{g}}_2$ with $\underline{\mathbf{g}}_1 = \underline{\mathbf{f}}_1$, and h($\underline{\mathbf{h}}_1$, $\underline{\mathbf{h}}_2$) and with $\underline{\mathbf{h}}_2$, $\underline{\mathbf{f}}_2$ (Fig. 21.5).

The strain increment $\underline{\underline{\mathbf{d\varepsilon}}}$ from time t^n to time t^{n+1} is computed by the code in the GN frame. It is expressed in the two frames g and h:

$$\underline{\underline{\mathbf{d\varepsilon}}} = \mathrm{d}\varepsilon^{\mathrm{g}}_{\alpha\beta}\ \underline{\mathbf{g}}_\alpha \otimes \underline{\mathbf{g}}_\beta = \mathrm{d}\varepsilon^{\mathrm{h}}_{\alpha\beta}\ \underline{\mathbf{h}}_\alpha \otimes \underline{\mathbf{h}}_\beta \tag{21.7}$$

where α and β are indexes taking value 1 or 2. The fibre stretching strain and the shear strain in the two frames are calculated:

$$\mathrm{d}\varepsilon^{\mathrm{g}}_{11} = \underline{\mathbf{g}}_1 \cdot \underline{\underline{\mathbf{d\varepsilon}}} \cdot \underline{\mathbf{g}}_1 \quad \mathrm{d}\varepsilon^{\mathrm{g}}_{12} = \underline{\mathbf{g}}_1 \cdot \underline{\underline{\mathbf{d\varepsilon}}} \cdot \underline{\mathbf{g}}_2 \tag{21.8}$$

$$\mathrm{d}\varepsilon^{\mathrm{g}}_{22} = \underline{\mathbf{h}}_2 \cdot \underline{\underline{\mathbf{d\varepsilon}}} \cdot \underline{\mathbf{h}}_2 \quad \mathrm{d}\varepsilon^{\mathrm{g}}_{12} = \underline{\mathbf{h}}_1 \cdot \underline{\underline{\mathbf{d\varepsilon}}} \cdot \underline{\mathbf{h}}_2 \tag{21.9}$$

The axial stress component and shear stress components are then computed:

$$\mathrm{d}\sigma^{\mathrm{g}}_{11} = E^{\mathrm{g}}\,\mathrm{d}\varepsilon^{\mathrm{g}}_{11} \quad \mathrm{d}\sigma^{\mathrm{g}}_{12} = G\mathrm{d}\varepsilon^{\mathrm{g}}_{12} \tag{21.10}$$

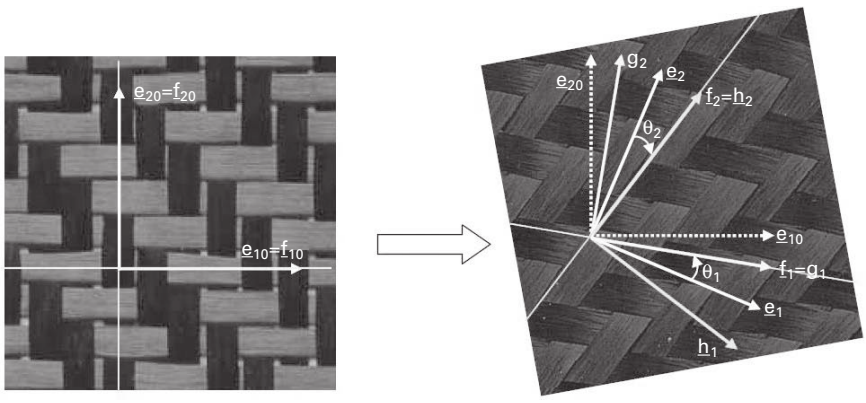

21.5 Fibre axes and GN axes in initial state and after deformation.

$$d\sigma_{22}^{h} = E^{h}\, d\varepsilon_{22}^{h} \quad d\sigma_{12}^{h} = G d\varepsilon_{12}^{h} \tag{21.11}$$

where E^{g} and E^{h} represent the tensile stiffness in the warp and weft fibre directions and G is the in-plane shear stiffness of the fabric. (They are not constant; G especially depends strongly on the in-plane shear.) The stresses are then integrated on the time increment from time t^{n} to time t^{n+1}:

$$(\sigma_{11}^{g})^{n+1} = (\sigma_{11}^{g})^{n} + d\sigma_{11}^{g\,n+1/2} \quad (\sigma_{12}^{g})^{n+1} = (\sigma_{12}^{g})^{n} + d\sigma_{12}^{g\,n+1/2} \tag{21.12}$$

$$(\sigma_{11}^{h})^{n+1} = (\sigma_{11}^{h})^{n} + d\sigma_{11}^{h\,n+1/2} \quad (\sigma_{12}^{h})^{n+1} = (\sigma_{12}^{h})^{n} + d\sigma_{12}^{h\,n+1/2} \tag{21.13}$$

The addition of the stresses in the warp and weft frames gives the stress in the fabric at time t^{n+1}:

$$\underline{\underline{\boldsymbol{\sigma}}}^{n+1} = (\underline{\underline{\boldsymbol{\sigma}}}^{g})^{n+1} + (\underline{\underline{\boldsymbol{\sigma}}}^{h})^{n+1} \tag{21.14}$$

More detail on this approach can be found in Khan *et al*. (2010). This approach is used to simulate the forming of a double dome shape corresponding to an international benchmark (Woven Composites Benchmark Forum, 2004). An experimental device has been constructed in INSA Lyon in order to perform this forming (Fig. 21.6). The woven fabric is a commingled glass/polypropylene plain weave which was tested in the material benchmark study conducted recently (Cao *et al*., 2008). The computed and experimental geometries after forming are compared in Fig. 21.6. The measured and numerical draw-in and shear angles agree (Figs 21.7 and 21.8) (Khan *et al*., 2010).

21.3.2 Hyperelastic model

For this approach (Aimène *et al*., 2010) a potential is defined which aims to reproduce the non-linear mechanical behaviour of textile composite reinforcements. The proposed potential is a function of the right Cauchy Green deformation tensor and structural tensor invariants defined from the fibre directions. This potential is based on the assumption that tensile and shear strain energies are uncoupled, and is the sum of three terms:

$$W = \overline{W}_{1}(I_{1}) + \overline{W}_{2}(I_{2}) + \overline{W}_{S}(I_{12}) \tag{21.15}$$

This assumption (that tensile and shear strain energies are uncoupled) is made for the sake of simplicity. The independence of tensile behaviour relative to in-plane shear has been shown experimentally (Buet-Gautier and Boisse, 2001). The other hypotheses are probably less true, but there is very little data available on the couplings.

The structural tensors $\underline{\underline{\mathbf{L}}}_{\alpha\beta}$ are defined from the two unit vectors in the warp and weft directions $\underline{\mathbf{f}}_{10}$ and $\underline{\mathbf{f}}_{20}$ in the reference configuration:

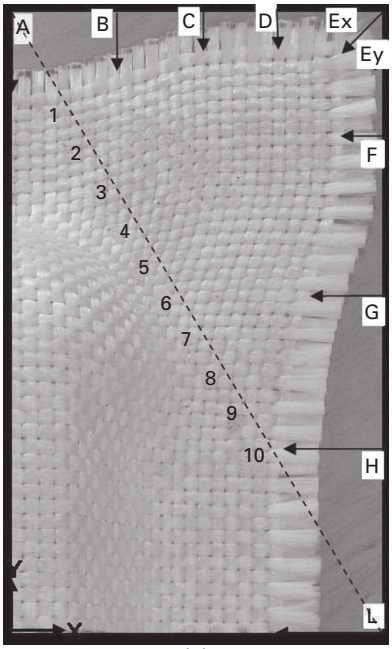

(a)

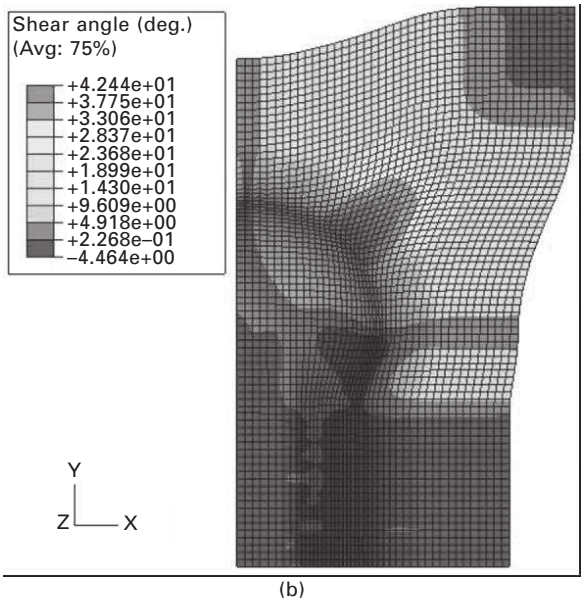

(b)

21.6 Location of points for material draw-in and shear angle measurement.

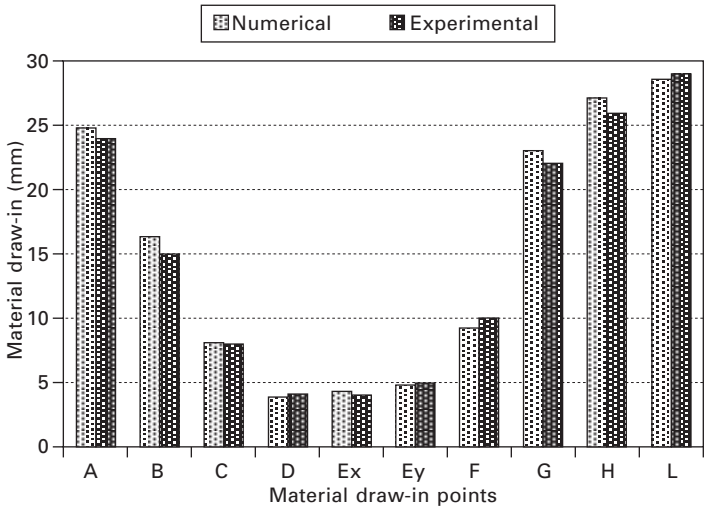

21.7 Comparison of material draw-in for the draped double dome.

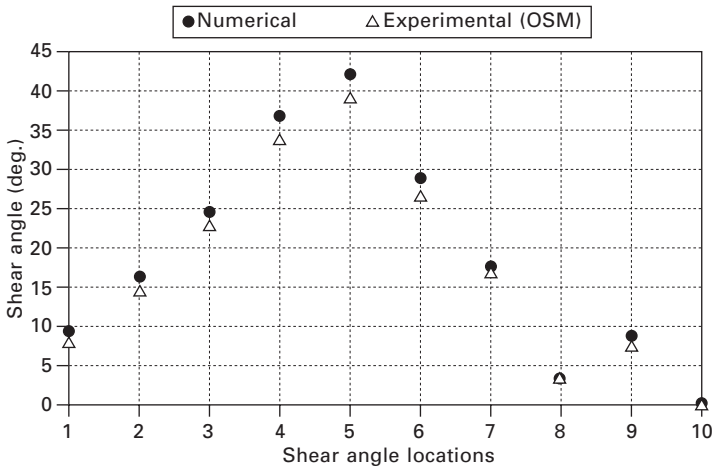

21.8 Comparison of shear angle of numerical and experimental outputs.

$$\underline{\underline{L}}_{\alpha\beta} = \underline{f}_{\alpha 0} \otimes \underline{f}_{\beta 0} \qquad 21.16$$

The two first terms $\overline{W}_1$ and $\overline{W}_2$ are the energies created by the tensions in the yarns. They are also functions of invariants I_1 and I_2 respectively themselves, depending on the right Cauchy–Green strain tensor $\underline{\underline{C}} = \underline{\underline{F}}^T \cdot \underline{\underline{F}}$ and the structural tensors $\underline{\underline{L}}_{\alpha\alpha}$:

$$I_1 = \mathrm{tr}(\underline{\underline{C}} \cdot \underline{\underline{L}}_{11}) = \lambda_1^2 \quad I_2 = \mathrm{tr}(\underline{\underline{C}} \cdot \underline{\underline{L}}_{22}) = \lambda_2^2 \tag{21.17}$$

where λ_α is the deformed length of a fibre with a unit initial length in the direction α.

The third term $\overline{W}_S$ is a function of the second mixed invariants of $\underline{\underline{C}}$.

$$I_{12} = \frac{1}{I_1 I_2} \mathrm{tr}(\underline{\underline{C}} \cdot \underline{\underline{L}}_{11} \cdot \underline{\underline{C}} \cdot \underline{\underline{L}}_{22}) = \cos^2\theta \tag{21.18}$$

The second Piola–Kirchhoff stress tensor is derived using this equation for the potential:

$$\underline{\underline{S}} = 2\left[\frac{\partial \overline{W}}{\partial I_1} - \frac{I_{12}}{I_1}\frac{\partial \overline{W}}{\partial I_{12}}\right]\underline{\underline{L}}_{11} + 2\left[\frac{\partial \overline{W}}{\partial I_2} - \frac{I_{12}}{I_2}\frac{\partial \overline{W}}{\partial I_{12}}\right]\underline{\underline{L}}_{22}$$

$$+ 2\left[\sqrt{\frac{I_{12}}{I_1 I_2}}\frac{\partial \overline{W}}{\partial I_{12}}\right](\underline{\underline{L}}_{12} + \underline{\underline{L}}_{21}) \tag{21.19}$$

The potential has to vanish in a stress-free configuration. Polynomial functions of the invariants are discussed in this chapter. The global form of the proposed potential energy is given by:

$$W(\underline{\underline{C}}) = \sum_{i=0}^{r} \frac{1}{i+1} A_i (I_1^{i+1} - 1) + \sum_{j=0}^{s} \frac{1}{j+1} B_j (I_2^{j+1} - 1) + \sum_{k=1}^{t} \frac{1}{k} C_k I_{12}^k \tag{21.20}$$

To determine the constants A_i, B_j and C_k, three experimental tests are necessary: two tensile tests in the warp and weft directions and one in-plane pure shear test.

The proposed hyperelastic model is implemented in a user routine VUMAT of Abaqus/Explicit and it is then applied to membrane elements. The simulation of a hemispherical punch forming process is performed in the case of strongly unbalanced twill. The warp rigidity is 50 N/yarn and the weft rigidity is 0.2 N/yarn. The experimental results in terms of a deformed shape are shown in Fig. 21.9(a) together with the results of the simulation in Fig. 21.9(b) and (c). The hyperelastic model is described in detail in Aimène *et al.* (2010).

21.4 The semi-discrete approach

This approach (Boisse *et al.*, 1997; Hamila *et al.*, 2009), which is relatively intermediate between the continuous and discrete approaches, obtains the textile composite reinforcement from a set of unit woven cells which bear the loads of their neighbouring cells (Fig. 21.10).

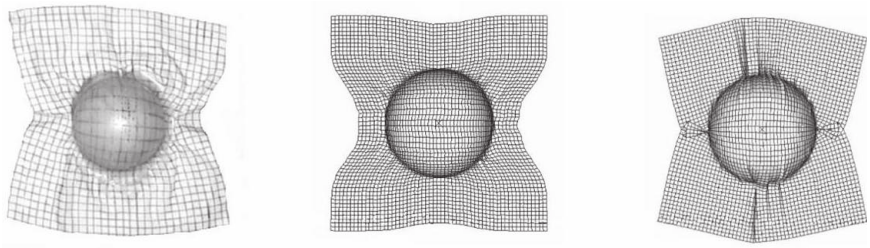

21.9 Deformed shape of an unbalanced fabric with an initial orientation of fibres 0°/90): (a) experimental shape; (b) Simulation without shear rigidity; (c) Simulation with shear rigidity.

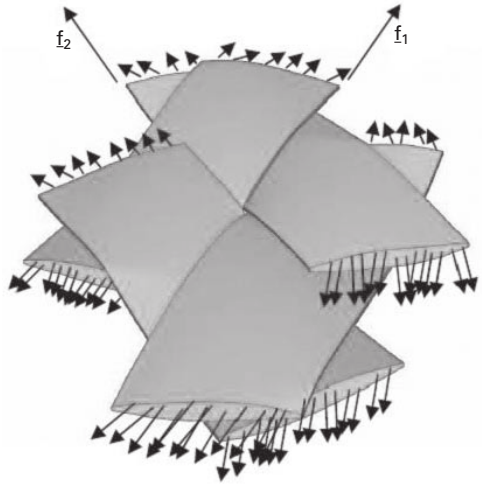

21.10 Loads on a unit woven cell.

- The tensions T_1 and T_2 are the resultants of the respective loads on warp and weft yarns in the directions $\underline{f}_1$ and $\underline{f}_2$ of these yarns (Fig. 21.11(a)).
- The in-plane shear moment M_s is the moment resulting from the loads on the unit woven cell at its centre, in the direction normal to the fabric (Fig. 21.11(b)).
- The bending moments M_1 and M_2 are the moments resulting from the loads on the warp and weft yarns respectively (Fig. 21.11(c)).

Figures 21.10 and 21.11 have been drawn to represent a plain weave for simplicity, but the type of weaving can vary.

In any virtual displacement field $\underline{\eta}$ such as $\underline{\eta} = 0$ on the boundary with prescribed displacements, the principle of virtual work compels the virtual

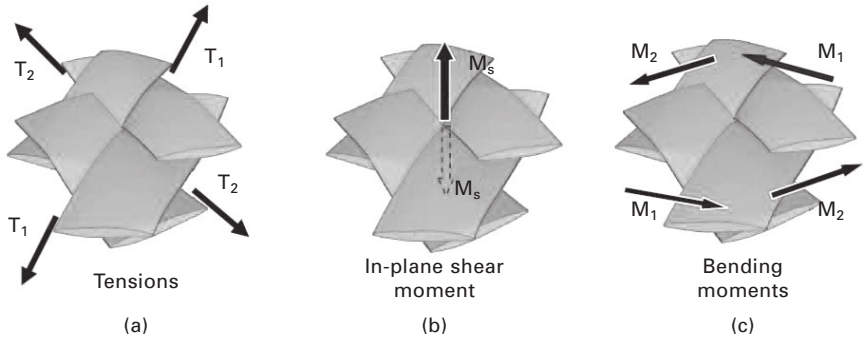

21.11 Load resultants on a unit woven cell.

inertial work to be equal to the difference between virtual internal and external works:

$$W_{\text{ext}}(\underline{\eta}) - W_{\text{int}}(\underline{\eta}) = W_{\text{acc}}(\underline{\eta}) \tag{21.21}$$

with

$$W_{\text{int}}(\underline{\eta}) = W_{\text{int}}^{\text{t}}(\underline{\eta}) + W_{\text{int}}^{\text{s}}(\underline{\eta}) + W_{\text{int}}^{\text{b}}(\underline{\eta}) \tag{21.22}$$

where $W_{\text{int}}^{\text{t}}(\underline{\eta})$, $W_{\text{int}}^{\text{s}}(\underline{\eta})$ and $W_{\text{int}}^{\text{b}}(\underline{\eta})$ are the virtual internal works of tension, in-plane shear and bending respectively:

$$W_{\text{int}}^{\text{t}}(\underline{\eta}) = \sum_{p=0}^{ncell} {}^{p}\varepsilon_{11}(\underline{\eta})\,{}^{p}T_1\,{}^{p}L_1 + {}^{p}\varepsilon_{22}(\underline{\eta})\,{}^{p}T_2\,{}^{p}L_2 \tag{21.23}$$

$$W_{\text{int}}^{\text{s}}(\underline{\eta}) = \sum_{p=1}^{ncell} {}^{p}\gamma(\underline{\eta})\,{}^{p}M_{\text{s}} \tag{21.24}$$

$$W_{\text{int}}^{\text{b}}(\underline{\eta}) = \sum_{p=1}^{ncell} {}^{p}\chi_{11}(\underline{\eta})\,{}^{p}M_1\,{}^{p}L_1 + {}^{p}\chi_{22}(\underline{\eta})\,{}^{p}M_2\,{}^{p}L_2 \tag{21.25}$$

where *ncell* denotes the number of woven cells, L_1 and L_2 the lengths of unit woven cells in the warp and weft directions, $\varepsilon_{11}(\underline{\eta})$ and $\varepsilon_{22}(\underline{\eta})$ the virtual axial strain in the warp and weft directions, $\gamma(\underline{\eta})$ the virtual in-plane shear angle, i.e the virtual angle variation between warp and weft directions, and $\chi_{11}(\underline{\eta})$ and $\chi_{22}(\underline{\eta})$ represent the virtual curvatures of the warp and weft directions. The quantity A is denoted ${}^{p}A$ when it concerns the unit woven cell number p. $\varepsilon_{11}(\underline{\eta})$, $\varepsilon_{22}(\underline{\eta})$, $\gamma(\underline{\eta})$, $\chi_{11}(\underline{\eta})$ and $\chi_{22}(\underline{\eta})$ are functions of the gradient of the virtual displacement field. T_1, T_2, M_{s}, M_1 and M_2 are the load results on the woven cell as presented above and in Fig. 21.11.

Experimental tests specific to textile composite reinforcements are used to obtain these mechanical properties. The biaxial tensile test gives the tensions

T_1 and T_2 as functions of the axial strains ε_{11} and ε_{22} (Kawabata *et al.*, 1973; Buet-Gautier and Boisse, 2001); the picture frame or the bias extension test gives the shear moment M_s as a function of the angle variation γ between warp and weft yarns (Wang *et al.*, 1998; Potter, 2002; Potluri *et al.*, 2006; Lomov *et al.*, 2006; Launay *et al.*, 2008; Cao *et al.*, 2008); and the bending test gives the bending moments M_1 and M_2 as respective functions of χ_{11} and χ_{22} (Kawabata, 1986; de Bilbao *et al.*, 2010). Virtual tests, for example 3D simulations of the deformation of a unit woven cell submitted to elementary loadings such as biaxial tensions or in-plane shear (Badel *et al.*, 2008, 2009) are an alternative to these experimental tests.

The approach presented in equations 21.1–21.5 assumes that the internal load state in the material is given by the membrane and bending resultant loads. It is restricted to thin reinforcements. This is true for a large section of composite reinforcements.

The five load resultants T_1, T_2, M_s, M_1 and M_2 can depend on the five kinematic quantities ε_{11}, ε_{22}, γ, χ_{11} and χ_{22}. Such knowledge is generally not available (and probably not often necessary). When considering in-plane shear, some studies have shown that the shear force can depend on the tension state (Lomov and Verpoest, 2006; Launay *et al.*, 2008). Such data is not usually available, however, and it is assumed that the picture-frame (or the bias-extension test) gives M_s only depending on γ.

A three-node shell finite element $M_1M_2M_3$ made up of *ncell* woven cells is shown in Fig. 21.12. The vectors $\underline{k}_1 = \underline{AM}_2$ and $\underline{k}_2 = \underline{BM}_3$ in the warp and weft directions respectively are defined. The internal virtual work of tension on the element (equation 21.23) defines the element nodal tensile internal forces $\mathbf{F}_{\text{int}}^{\text{te}}$:

$$\sum_{p=1}^{ncell} {}^p\varepsilon_{11}(\underline{\eta})\,{}^pT_1\,{}^pL_1 + {}^p\varepsilon_{22}(\underline{\eta})\,{}^pT_2\,{}^pL_2 = \boldsymbol{\eta}^{\text{eT}}\mathbf{F}_{\text{int}}^{\text{te}} \qquad 21.26$$

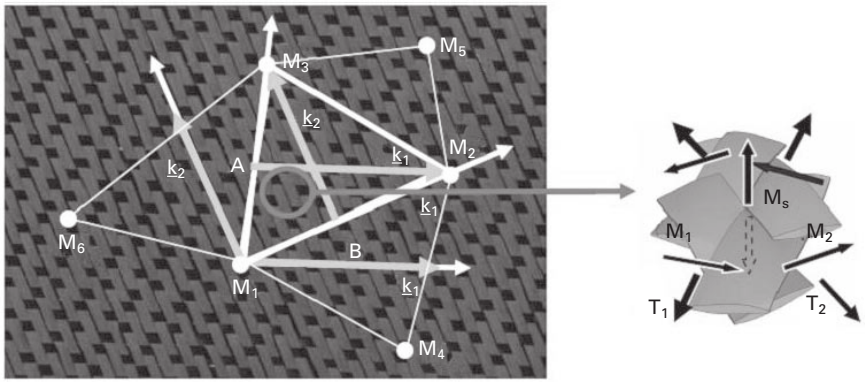

21.12 Three-node finite element made of unit woven cells.

The internal tensile force components are calculated from the tensions of T_1 and T_2:

$$(\mathrm{F}_{\mathrm{int}}^{\mathrm{te}})_{ij} = ncell \left(B_{1ij} T_1 \frac{\mathrm{L}_1}{\left\| \underline{k}_1 \right\|^2} + B_{2ij} T_2 \frac{\mathrm{L}_2}{\left\| \underline{k}_2 \right\|^2} \right) \qquad 21.27$$

where i represents the index of the direction (i = 1 to 3) and j is the index of the node (j = 1 to 3). B_{1ij} and B_{2ij} are strain interpolation components. They are constant over the element because the interpolation functions are linear in the case of the three-node triangle.

The internal virtual work of in-plane shear on the element (equation 21.24) defines the element nodal tensile internal forces $\mathbf{F}_{\mathrm{int}}^{\mathrm{se}}$:

$$\sum_{p=1}^{ncell} {}^{p}\gamma(\underline{\eta})\, {}^{p}M_{\mathrm{s}} = \boldsymbol{\eta}^{\mathrm{eT}} \mathbf{F}_{\mathrm{int}}^{\mathrm{se}} \qquad 21.28$$

The internal in-plane shear force components are calculated from the in-plane shear moment:

$$(\mathrm{F}_{\mathrm{int}}^{\mathrm{se}})_{ij} = ncell\ B_{\gamma ij}\, M_{\mathrm{s}}(\gamma) \qquad 21.29$$

In order to avoid supplementary degrees of freedom and consequently to improve numerical efficiency, the bending stiffness is taken into account within an approach without a rotational degree of freedom (Onate and Zarate, 2000; Sabourin and Brunet, 2006). In these approaches the curvatures of the element are computed from the positions and displacements of the nodes of the neighbouring elements (Fig. 21.12). The internal virtual work of bending on the element (equation 21.25) defines the element nodal bending internal forces $\mathbf{F}_{\mathrm{int}}^{\mathrm{be}}$:

$$\sum_{p=1}^{ncell} {}^{p}\chi_{11}(\underline{\eta})\, {}^{p}M_1\, {}^{p}L_1 + {}^{p}\chi_{22}(\underline{\eta})\, {}^{p}M_2\, {}^{p}L_2 = \boldsymbol{\eta}^{\mathrm{eT}}\, \mathbf{F}_{\mathbf{int}}^{\mathrm{be}} \qquad 21.30$$

The internal bending force components are calculated from the bending moments M_1 and M_2:

$$(\mathrm{F}_{\mathrm{int}}^{\mathrm{be}})_{\mathrm{km}} = ncell \left(Bb_{1\mathrm{km}} M_1 \frac{L_1}{\left\| \underline{k}_1 \right\|^2} + Bb_{2\mathrm{km}}\, M_2 \frac{L_2}{\left\| \underline{k}_2 \right\|^2} \right) \qquad 21.31$$

The details of the calculations of the internal loads can be found in Hamila *et al.* (2009).

Figure 21.13 shows the simulation of the deep drawing of a woven reinforcement with a cylindrical punch (Boisse *et al.*, 2011). It uses the semi-discrete approach presented above. Height-independent blank holders

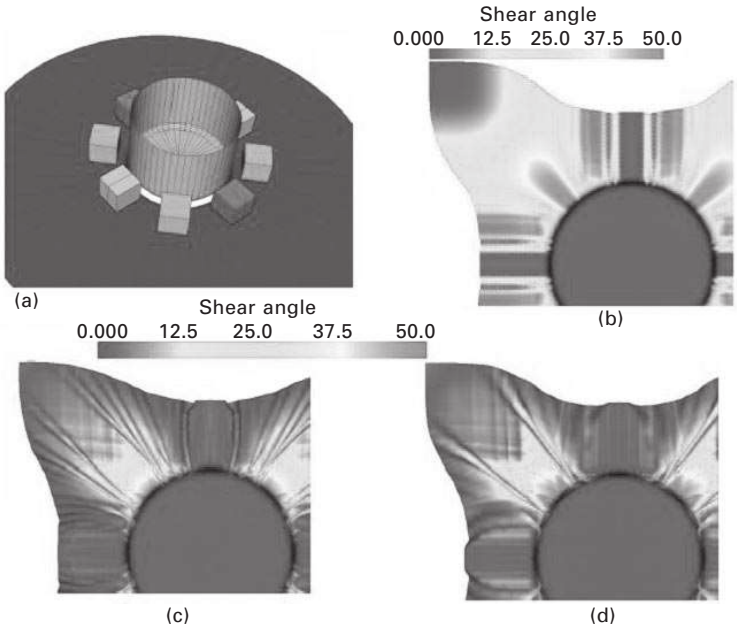

21.13 Forming with a cylindrical punch: (a) geometry of the tools; (b) tensile stiffness only; (c) small bending stiffness; (d) higher bending stiffness.

are shown in Fig. 21.13(a), and Fig. 21.13(b) shows the computed deformed shape of the reinforcement when only the tensile stiffness is taken into account. There is no wrinkle and the computed shear angles are very large. They reach 70°. Figures 21.13(c) and 21.13(d) show the computed deformed shape when all the rigidities (tensile, in-plane shear and bending) have been considered. The bending stiffness is 10 times larger in Fig. 21.13(d) than in Fig. 21.13(c). There are many wrinkles in both cases, especially between the blank-holders. These wrinkles are less numerous and their size is moderately larger when the bending stiffness increases.

The simulation of the hemispherical forming of a very unbalanced fabric is shown in Fig. 21.14 (Boisse *et al.*, 2011). There is a 250° ratio between the tensile stiffness in the warp and weft directions. A 6 kg ring was used as blank-holder to avoid reinforcement wrinkling in the curved zone (Fig. 21.4(a)). The experimental shape obtained after forming is shown in Fig. 21.14(e) (Daniel *et al.*, 2003). In the warp-direction image, large fabric sliding is observed relative to the die, whereas, contrastingly, in the weft direction (the weaker direction) no edge movement is depicted and the yarns were subjected to large stretch deformations. A 6 kg ring was used as blank-holder to avoid reinforcement wrinkling in the curved zone (Fig. 21.14(a)).

The shapes after forming are shown in Figs 21.14(b), (c) and (d) for

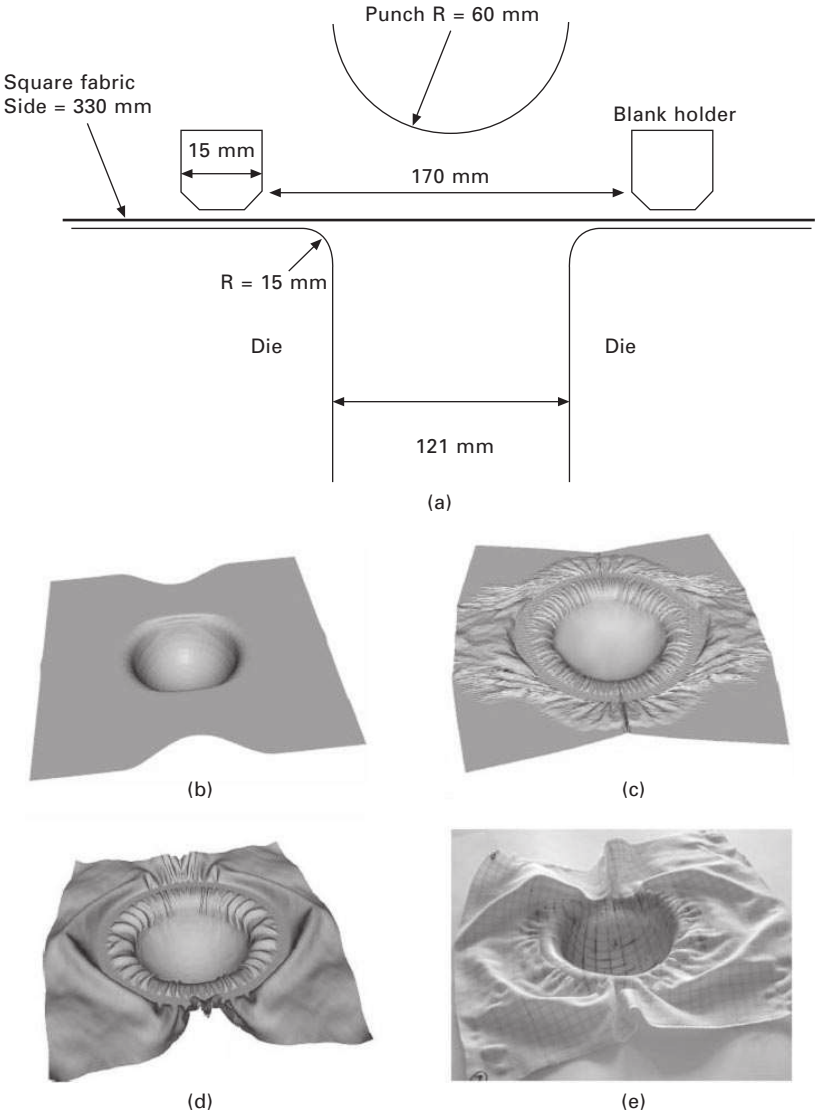

21.14 Forming of an unbalanced textile reinforcement: (a) geometry of the tools; (b) tensile stiffness only; (c) tensile and in-plane shear rigidities; (d) tensile + in-plane shear + bending rigidities; (e) experimental forming.

different types of simulations. The tensile stiffness is taken into account only in Fig. 21.14(b). There is no wrinkle, but the asymmetry of the shape in the warp and weft directions is correctly obtained. In Fig. 21.14(c) tension and in-plane shear strain energies, but not bending stiffness, are taken into

account. A great number of small wrinkles are depicted. The wrinkles are much bigger in Fig. 21.14(d) where the bending stiffness is added. The shapes of these wrinkles conform fairly well with the expectations of the experiment. Near the central point of the preform, squares drawn on the fabric prior to forming become rectangles with a length:width ratio of 1:8 (Fig. 21.14(e)). This extension ratio is correctly computed in the three cases shown in (Fig. 21.14(b), (c) and (d)). It depends on the tensile rigidities which are taken into account in all three cases. Interestingly, a fishnet algorithm which ignored the mechanical properties would lead to the same deformation in both warp and weft directions and the ratio in the central part would remain equal to 1.

21.5 Discussion and conclusion

The discrete (or mesoscopic) approach is both attractive and promising. The very specific mechanical behaviour of the textile material due to the contacts and friction between the yarns and to the change of direction is implicitly taken into account. If some sliding occurs between warp and weft yarns, they can be simulated. This is not possible when using the continuous approaches, which consider the textile material as a continuum. This is an important point because it can be necessary to prevent such a sliding in a process. Nevertheless, the main drawback of the discrete approach is the necessary compromise that must be made between the accuracy of the model of the unit woven cell and the total number of degrees of freedom. The modelling of the unit cell must be accurate enough to obtain a correct macroscopic mechanical behaviour, but the number of degrees of freedom of each cell must remain small in order to compute a forming process for which there will be thousands of woven cells. The continuous approach is the most commonly used method in composite reinforcement forming today. Its main advantage is that standard shell or membrane finite elements can be used. It is only the mechanical behaviour which has to be specified in order to take the very particular behaviour of textile materials into account. Many models exist, but none of them are clearly defined yet. The semi-discrete approach aims to avoid the use of stress tensors and directly define the loading onto a woven unit cell using the warp and weft tensions and by in-plane shear and bending moments. These quantities are simply defined on a woven unit cell and above all they are directly measured by standard tests on composite reinforcements.

21.6 Acknowledgements

The work reported here has been carried out partly thanks to the scope of the LCM3M and MECAFIBRES projects by the National French Agency for Research ANR.

21.7 References

Advani SG (1994) *Flow and Rheology in Polymeric Composites Manufacturing*. Elsevier, Amsterdam.

Aimène Y, Vidal-Sallé E, Hagège B, Sidoroff F, Boisse P (2010) A hyperelastic approach for composite reinforcement large deformation analysis. *Journal of Composite Materials* 44(1): 5–26.

Allaoui S, Boisse P, Chatel S, Hamila N, Hivet G, Soulat D, Vidal-Sallé E (2011) Experimental and numerical analyses of textile reinforcement forming of a tetrahedral shape. *Composites: Part A*, 42: 612–622.

Badel P, Vidal-Sallé E, Maire E, Boisse P (2008) Simulation and tomography analysis of textile composite reinforcement deformation at the mesoscopic scale. *Composites Science and Technology* 68: 2433–2440.

Badel P, Gautier S, Vidal-Sallé E, Boisse P (2009) Rate constitutive equations for computational analyses of textile composite reinforcement mechanical behaviour during forming. *Composites: Part A* 40: 997–1007.

Boisse P, Borr M, Buet K, Cherouat A (1997) Finite element simulations of textile composite forming including the biaxial fabric behaviour. *Composites: Part B Engineering Journal* 28B: 453–464.

Boisse P, Hamila N, Vidal-Sallé E, Dumont F (2011) Simulation of wrinkling during textile composite reinforcement forming. Influence of tensile, in-plane shear and bending stiffnesses. *Composites Science and Technology*, 71: 683–692.

Buet-Gautier K, Boisse P (2001) Experimental analysis and modeling of biaxial mechanical behavior of woven composite reinforcements. *Experimental Mechanics* 41: 260–269.

Cao J, Akkerman R, Boisse P, Chen J *et al*. (2008) Characterization of mechanical behavior of woven fabrics: Experimental methods and benchmark results. *Composites: Part A* 39: 1037–1053.

Dafalias YF (1983) Corotational rates for kinematic hardening at large plastic deformations. *Transactions of the ASME, Journal of Applied Mechanics* 50: 561–565.

Daniel JL, Soulat D, Dumont F, Zouari B, Boisse P, Long AC (2003) Forming simulation of very unbalanced woven composite reinforcements. *International Journal of Forming Processes* 6(3–4): 465–480.

de Bilbao E, Soulat D, Hivet G, Gasser A (2010) Experimental study of bending behaviour of reinforcements. *Experimental Mechanics* 50: 333–351.

de Luycker E, Morestin F, Boisse P, Marsal D (2009) Simulation of 3D interlock composite preforming. *Composite Structures* 88: 615–623.

Duhovic M, Bhattacharyya D (2006) Simulating the deformation mechanisms of knitted fabric composites. *Composites: Part A* 37: 1897–1915.

Dumont F, Weimer C, Soulat D, Launay J, Chatel S, Maison-Le-Poec S (2008) Composite preform simulations for helicopter parts. *International Journal of Materials Forming* Suppl 1, 847–850.

Durville D (2005) Numerical simulation of entangled materials mechanical properties. *Journal of Materials Science* 40: 5941–5948.

Gatouillat S (2010) Approche mésoscopique pour la mise en forme des renforts de composites tissés. PhD thesis, INSA Lyon, France.

Green AE, Naghdi PM (1965) A general theory of an elastic–plastic continuum. *Archives of Rational Mechanical Analysis* 18: 251–281.

Hamila N, Boisse P, Sabourin F, Brunet M (2009) A semi-discrete shell finite element

for textile composite reinforcement forming simulation. *International Journal of Numerical Methods in Engineering* 79: 1443–1466.

Hammami A, Trochu F, Gauvin R, Wirth S (1996) Directional permeability measurement of deformed reinforcement. *Journal of Reinforced Plastic Composites* 15:. 552–562.

ITOOL 'Integrated Tool for Simulation of Textile Composites'. European specific targeted research project, sixth framework programme, aeronautics and space, <http://www.itool.eu>

Kawabata S (1986) *The Standardization and Analysis of Hand Evaluation*, 2nd edn. The Textile Machinery Society of Japan, Osaka, Japan.

Kawabata S, Niwa M, Kawai H (1973) The finite deformation theory of plain weave fabrics, part I: the biaxial deformation theory. *Journal of the Textile Institute* 64(1): 21–46.

Khan MA, Mabrouki T, Vidal-Sallé E, Boisse P (2010) Numerical and experimental analyses of woven composite reinforcement forming using a hypoelastic behaviour. Application to the double dome benchmark. *Journal of Materials Processing Technology* 210: 378–388.

Launay J, Hivet G, Duong AV, Boisse P (2008) Experimental analysis of the influence of tensions on in plane shear behaviour of woven composite reinforcements. *Composites Science and Technology* 68: 506–515.

Loix F, Badel P, Orgéas L, Geindreau C, Boisse P (2008) Woven fabric permeability: from textile deformation to fluid flow mesoscale simulations. *Composites Science and Technology* 68: 1624–1630.

Lomov SV, Verpoest I (2006) Model of shear of woven fabric and parametric description of shear resistance of glass woven reinforcements. *Composites Science and Technology* 66: 919–933.

Lomov SV, Willems A, Verpoest I, Zhu Y, Barburski M, Stoilova Tz (2006) Picture frame test of woven composite reinforcements with a full-field strain registration. *Textile Research Journal* 76(3): 243–252.

Miao Y, Zhou E, Wang Y, Cheeseman BA (2008) Mechanics of textile composites: Micro-geometry. *Composites Science and Technology* 68: 1671–1678.

Onate E, Zarate F (2000) Rotation-free triangular plate and shell elements. *International Journal for Numerical Methods in Engineering* 47: 557–603.

Parnas RS (2000) *Liquid Composite Molding*, Hanser Gardner Publications, Cincinnati, OH.

Peng X, Cao J (2005) A continuum mechanics-based non-orthogonal constitutive model for woven composite fabrics. *Composites: Part A* 36: 859–874.

Pickett AK, Creech G, de Luca P (2005) Simplified and advanced simulation methods for prediction of fabric draping. *European Journal of Computational Mechanics* 14: 677–691.

Potluri P, Perez Ciurezu DA, Ramgulam RB (2006) Measurement of meso-scale shear deformations for modelling textile composites. *Composites: Part A* 37: 303–314.

Potter K (2002) Bias extension measurements on cross-plied unidirectional prepreg. *Composites: Part A* 33: 63–73.

Sabourin F, Brunet M (2006) Detailed formulation of the rotation-free triangular element 'S3' for general purpose shell analysis. *Engineering Computations* 23(5): 469–502.

Spencer AJM (2000) Theory of fabric-reinforced viscous fluids. *Composites: Part A* 31: 1311–1321.

ten Thije RHW, Akkerman R, Huétink J (2007) Large deformation simulation of anisotropic

material using an updated Lagrangian finite element method. *Computer Methods in Applied Mechanics in Engineering* 196: 3141–3150.

Wang J, Page JR, Paton R (1998) Experimental investigation of the draping properties of reinforcement fabrics. *Composites Science and Technology* 58: 229–237.

Woven Composites Benchmark Forum (2004) http://www.wovencomposites.org/index.php?show=comment&catgid=4&topicid=37

Index